

---

# NONAXISYMMETRIC INSTABILITIES IN SELF-GRAVITATING DISKS. II LINEAR AND QUASI-LINEAR ANALYSES

Kathryn Z. Hadley, Paul Fernandez, James N. Imamura, Erik Keever, Rebecka Tumblin, & William Dumas

*Accepted for publication in Astrophysics and Space Science*

**Abstract** We studied global nonaxisymmetric hydrodynamic instabilities in an extensive collection of hot, self-gravitating polytropic disk systems, systems that covered a wide expanse of the parameter space relevant to protostellar and protoplanetary systems. We examined equilibrium disk models varying three parameters: the ratio of the inner to outer equatorial radii, the ratio of star mass to disk mass, and the rotation law exponent  $q$ . We took the polytropic index  $n = 1.5$  and examined the exponents  $q = 1.5$  and 2, and the transitional one  $q = 1.75$ . For each of these sets of parameters, we examined models with inner to outer radius ratios from 0.1 to 0.75, and star mass to disk mass ratios from 0 to  $10^3$ . We numerically calculated the growth rates and oscillation frequencies of low-order nonaxisymmetric disk modes, modes with azimuthal dependence  $\propto e^{im\phi}$ . Low- $m$  modes are found to dominate with the character and strength of instability strongly dependent on disk self-gravity. Representatives of each mode type are examined in detail, and torques and mass transport rates are calculated.

## 1 INTRODUCTION

Star formation takes place in Giant Molecular clouds where collapse of small embedded cloud cores is triggered by external mechanisms such as shock waves or stellar winds. For nonrotating cloud cores, our understanding of the star formation process is well in hand. However, it is clear that in general, rotation

must be taken into account. Observations show that molecular cloud cores typically have specific angular momenta  $\sim 10^{21-22} \text{ cm}^2 \text{ s}^{-1}$  (*e.g.*, see Tohline 2002). Clouds with such high specific angular momenta cannot collapse directly into stars. Only a few percent of the cloud matter, that nearest the rotation axis, goes directly into the formation of the central object; the rest forms a massive circumstellar disk (*e.g.*, see Shu, Adams, & Lizano 1987, Tohline 2002). Star formation thus hinges on how mass from the disk finds its way onto the nascent star. Molecular viscosity as a mechanism is ineffective at transport of angular momentum in astrophysical disks. Other mechanisms are needed to enhance transport above that which results from binary particle collisions (Armitage 2011). Hydrodynamic and/or magnetohydrodynamic nonaxisymmetric instabilities have been proposed as ways to supply the needed dissipation, either directly through wave transport or indirectly as mechanisms that generate turbulence which supplies the needed effective viscosity (Balbus & Hawley 1998). We model the redistribution of angular momentum through global nonaxisymmetric hydrodynamic instabilities in this and follow-up papers. Recent reviews of the fluid mechanics involved in young stellar objects by Shariff (2009) and Armitage (2011) include summaries of observed characteristics of various classes of objects, as well as discussions of various mechanisms involved, focusing on magnetic field effects, radiation transport and turbulence.

The stability of nonmagnetic disks has been of interest since the late nineteenth century when Dyson (1893) first investigated what he called *anchor rings*. As with many systems in physics, the stability analyses began with simplified models, adding increasing complexity over time. Serious attempts at the stability analysis of non-self-gravitating thick disks began with Papaloizou & Pringle (1984, 1985) who studied isentropic disks with power law differential rotation. They made the

---

Kathryn Z. Hadley, Paul Fernandez, James N. Imamura, Erik Keever, Rebecka Tumblin, & William Dumas

Institute of Theoretical Science, University of Oregon, Eugene, OR 97403-1229

important discovery that disks may be dynamically unstable to global nonaxisymmetric modes with azimuthal dependence given by  $e^{im\phi}$ . For the special cases of a thin cylindrical shell and a thin isothermal ring, a threshold of instability was found for low- $m$  modes and slender tori such that disks were found to be unstable for a range of angular momentum profiles. For disks with power law angular rotation distributions with exponent  $q$ , Kelvin-Helmholtz-like instabilities were found to dominate disks for low  $q$  while sonic instability dominates systems near a constant specific angular momentum profile,  $q = 2$ . These sonic instabilities were later named P modes. Papaloizou & Pringle (1987) subsequently performed work on higher order modes, studying modes trapped near the inner and outer disk boundaries by an evanescent region around corotation, modes for which the fluid speed equals the speed of the perturbation. Kojima (1986, 1989) further analyzed non-self-gravitating isentropic thick disks for  $q = 2$  and  $n = 0, 1.5$ , and  $3.0$ , where  $n$  is the polytropic index. Kojima found the disks were unstable for almost all cases calculated and that the growth rate decreased for either sufficiently large or small radial widths, and also decreased with decreasing  $q$ . The growth rates showed little dependence on compressibility, with only small differences between his  $n = 1.5$  and  $n = 3.0$  calculations.

The effect of self-gravity was first included in the analytic and numerical investigations of long wavelength modes found in slender, incompressible tori by Goldreich, Goodman & Narayan (1986). Their theory used a thin ribbon approximation to investigate the two-dimensional incompressible limit of the narrow torus. They showed that two new modes emerged, one with corotation at the density maximum, called the J mode (for the Jeans instability) and a second with corotation outside the ribbon, called the I mode (intermediate between P and J modes). Goodman & Narayan (1988) further investigated I modes and J modes adding self-gravity to their calculations of 3D slender incompressible tori with  $q = 2$  and two-dimensional slender incompressible tori with varying  $q$ . They found that I and J modes were strongly influenced by self-gravity showing character different from the P modes.

Papaloizou & Lin (1989) used a variational principle approach to study thin (flat) self-gravitating disks. They found modes which fell into three categories determined by the distribution of vortensity (see also Papaloizou & Savonije 1991). One kind of mode is associated with extrema in vortensity, corresponding to a disk where corotation is located at the radius of the maximum density. A second mode depicts modes generated by the gradient of vortensity on the disk boundaries,

corresponding to the existence of the corotation radius outside the disk. A third mode is associated with internal variations in the vortensity gradient. These modes show corotation inside the disk, but not necessarily at the density maximum.

An important development in the study of disks occurred when Adams, Ruden, & Shu (1989) showed that the *indirect* stellar potential could couple the star and disk, and drive one-armed spiral modes,  $m = 1$  modes in disks. Symmetry arguments showed that multi-armed modes with  $m \geq 2$  could not drive the central star off the disk center of mass and so could not contribute to the indirect stellar potential. Adams, Ruden & Shu (1989) found that  $m = 1$  modes were unstable for high mass disks ( $M_*/M_d \approx 1$ ), attributing instability to SLING amplification (however, see Heemskerk, Papaloizou, & Savonije 1991). Noh, Vishniac & Cochran (1992) studied  $m = 1$  modes in Keplerian ( $q = 1.5$ ) disks for high and low disk masses with emphasis on sensitivity to the outer disk boundary conditions. They found that low mass disks, down to  $M_*/M_d \approx 2.0$ , were unstable to  $m = 1$  modes only when a reflecting outer boundary existed, with growth rates increasing rapidly with an increase in disk mass and that there were two types of  $m = 1$  modes (see also Hadley & Imamura 2011).

Mathematically simple systems, such as infinitesimally thin disks, self-gravitating annuli and tori with constant mass density and circular cross-sections, have been studied extensively. Fully 3D, self-gravitating disks have received much less attention. Self-gravitating polytropic disks were analyzed by Eriguchi & Hachisu (1983) and Hachisu & Eriguchi (1985a, 1985b). Tohline & Hachisu (1990) performed nonlinear calculations for  $n = 1.5$ , varying  $q$ , for extremely small mass stars,  $10^{-9} < M_*/M_d < 10^{-6}$ , making these disks fully self-gravitating. Their analysis included eight models but was extended in a second paper, Woodward, Tohline & Hachisu (1994) where a more extensive study was performed, this time including models where the star-to-disk ratio was much larger. Hadley & Imamura (2011), performed linear stability analyses on self-gravitating toroids,  $M_*/M_d = 0.0$ . In addition, they modeled the early nonlinear evolution using a quasilinear theory and, for selected models, fully nonlinear techniques. In our present work, we perform an extensive study of nonaxisymmetric global instabilities in thick, self-gravitating star-disk systems creating a large catalog of star/disk systems covering most of the parameter space relevant to protostellar and protoplanetary systems. We consider star/disk systems for  $n = 1.5$ ,  $q = 1.5, 1.75$  and  $2$ , for star masses of  $0.0 \leq M_*/M_d \leq 10^3$  and inner to outer edge aspect

ratios of  $0.1 < r_-/r_+ < 0.75$ . We discuss how the trends found in the non-self-gravitating disks and thin disks systems carry over to self-gravitating thick disks, as well as how the extra degree of freedom leads to new behavior. We perform quasi-linear analysis and compare our linear and quasi-linear modeling results with nonlinear simulations in Paper III of this series (Hadley *et al.* 2014).

The remainder of our paper is organized as follows. Section 2 introduces our mathematical methods and concepts. Section 3 presents our results. Section 4 contains discussion and applications with comparison of our results with those of previous studies. Section 5 contains a summary of our results and conclusions.

## 2 EQUILIBRIUM DISKS

### 2.1 Equilibrium Disk Equations

The inviscid, adiabatic, hydrodynamic equations are

$$\partial_t \rho + \nabla \cdot (\rho \mathbf{v}) = 0 \quad (1)$$

and

$$\rho(\partial_t + \mathbf{v} \cdot \nabla) \mathbf{v} = -\nabla P - \rho \nabla \Phi_g \quad (2)$$

where  $P$  is the pressure,  $\rho$  is the mass density,  $\mathbf{v}$  is the velocity, and  $\Phi_g$  is the total gravitational potential composed of the disk self-gravitational potential,  $\Phi_d$ , and the stellar potential,  $\Phi_*$ . The disk potential is found from solution of the Poisson equation

$$\nabla^2 \Phi_d = 4\pi G \rho \quad (3)$$

where  $G$  is the gravitational constant. The stellar potential is found from the potential formula for a point mass

$$\Phi_* = -\frac{GM_*}{|\mathbf{r} - \mathbf{r}_*|}, \quad (4)$$

where  $\mathbf{r}$  is the field point and  $\mathbf{r}_*$  is the position of the star. In equilibrium,  $r_* = 0$ , but for the perturbed flow, we determine  $r_*$  using the stellar equation of motion given by

$$\frac{d\vec{v}_*}{dt} = -\nabla \Phi_d. \quad (5)$$

The perturbed form of the stellar equation of motion is given in equation 24.

We calculate equilibrium models using the self-consistent field method (SCF, Hachisu [1986]) under the following assumptions: (i) axial symmetry; (ii) the

fluid rotates on cylinders; and (iii) the disk has mirror symmetry across the equatorial plane. For isentropic fluids the relationship between  $P$  and  $\rho$  is  $P = K\rho^{1+1/n}$  where  $P$  is pressure,  $\rho$  is mass density,  $n$  is the polytropic index, and  $K$  is the polytropic constant. We investigate models with  $n = 1.5$ . The velocity field is defined using a power law angular velocity distribution

$$\Omega(\varpi) = \Omega_o \left( \frac{\varpi}{r_o} \right)^{-q} \quad (6)$$

where  $r_o$  is the radius of the density maximum,  $\Omega_o$  is the frequency of the fluid at  $r_o$ , and  $\varpi$  is the cylindrical radial coordinate. Keplerian rotation refers to  $q = 1.5$ , and the axisymmetrically neutrally-stable case of constant specific angular momentum is  $q = 2$ . Unless otherwise noted, all quantities are presented in polytropic units where  $G = K = M_d = 1$ ,  $G$  is the gravitational constant, and  $M_d$  is the the disk mass. Conversion between polytropic units and physical units can be made using transformations found in Williams & Tohline (1987).

The mass continuity equation is identically satisfied and the momentum conservation equation may be integrated once for axisymmetric disks that rotate on cylinders. In cylindrical coordinates we find

$$\frac{\gamma}{\gamma-1} K \rho^{1/n} - \frac{GM_*}{r} + \Phi_d - \int \Omega_o^2 r_o^{2q} \varpi^{1-2q} d\varpi - C = 0 \quad (7)$$

where  $\gamma = 1+1/n$ ,  $M_*$  is the mass of the star,  $C$  is the integration constant whose value is determined by the boundary conditions. Defining dimensionless variables

$$\psi = \frac{\rho}{\rho_o}, \quad \theta = \frac{\varpi}{r_o}, \quad \xi = \frac{r}{r_o}, \quad \varphi_d = \frac{\Phi_d}{\Phi_o}, \quad (8)$$

$$\text{and } \varphi_c = - \int \theta^{1-2q} d\theta$$

where  $\varphi_c$  is the centrifugal potential, we arrive at

$$\frac{\gamma}{\gamma-1} \psi^{1/n} - \left( \frac{M_*}{M_d} \right) \frac{1}{\xi} + \varphi_d + h_o^2 \varphi_c - C' = 0. \quad (9)$$

After setting

$$\frac{\Phi_o}{K\rho_o^{1/n}} = 1, \quad h_o^2 = \frac{\Omega_o^2 r_o^2}{K\rho_o^{1/n}}, \quad C' = \frac{C}{K\rho_o^{1/n}} \quad (10)$$

and using the Poisson equation to show that

$$\Phi_o = G\rho_o r_o^2 \rightarrow \frac{GM_*}{K\rho_o^{1/n} r_o} = \frac{M_*}{M_d}. \quad (11)$$

We solve Equation 9 as follows: (i) values for  $\psi$  are guessed; (ii)  $\varphi_d$  and  $\varphi_c$  are calculated; (iii) using  $\varphi_d$

and  $\varphi_c$ , Equation 9 is inverted for  $\psi$ ; (iv) if the guessed and calculated  $\psi$  agree to within a predetermined tolerance, the calculation is stopped. If they do not, the guess for  $\psi$  is improved and steps (ii) and (iii) repeated. This is continued until the guessed and calculated  $\psi$  are consistent. We use a global test for convergence by monitoring the changes in the constants  $h_c^2$  and  $C'$  from iteration to iteration. We quantified the accuracy of our result using the virial theorem,  $2(T + T_{th}) + W = 0$ , where  $T$  is the rotational kinetic energy,  $T_{th}$  is the kinetic energy in thermal motion, and  $W$  is the gravitational energy. In practice, this quantity does not equal zero. In general, our models had

$$VT = \left| \frac{T + T_{th} + 0.5W}{-0.5W} \right| < 10^{-3} - 10^{-4}, \quad (12)$$

However, for small  $M_*/M_d$  and large  $r_-/r_+$ , VT could be as large as 0.01.

## 2.2 Equilibrium Disk Properties

An extensive library of equilibrium disk models was compiled covering the parameter space occupied by typical protostellar and protoplanetary disks. Disk models were grouped into families defined by  $n$  and  $q$ , where family members were parameterized by  $r_-/r_+$ , the ratio of the inner and outer radii of the disk, and  $M_*/M_d$ , the ratio of the star mass disk mass. We modeled  $q = 1.5, 1.75$  and  $2$  disks for  $r_-/r_+ = 0.05$  to  $0.75$ , and  $M_*/M_d = 0$  to  $10^3$ . Density contours in meridional slices for representative models are shown in Figure 1 to qualitatively illustrate the effects of varying  $M_*/M_d$ ,  $q$  and  $r_-/r_+$ . Large star masses, small inner radii and shallow rotation curves all have the effect of flattening the disk. Small stars, large inner radii and steep rotation curves have the opposite effect leading to values of  $h/r \approx 1$  where  $h$  is the disk thickness at radius  $r$ . The latter is where we expect thin-disk approximations to break down.

We investigate disk stability based on local and global macroscopic properties of the equilibrium disks. Some examples of parameters include the well-known Toomre  $Q$  parameter which indicates local instability in thin disks if  $Q$  falls below unity, where

$$Q = \frac{c_s \kappa}{\pi G \Sigma}, \quad (13)$$

$c_s$  is the local sound speed, and  $\kappa$  is the epicyclic frequency,

$$\kappa^2 = (4 - 2q)\Omega^2 \quad (14)$$

for power law rotation (Toomre 1964). For nonaxisymmetric instability, a corresponding necessary and sufficient condition does not exist but it has been suggested

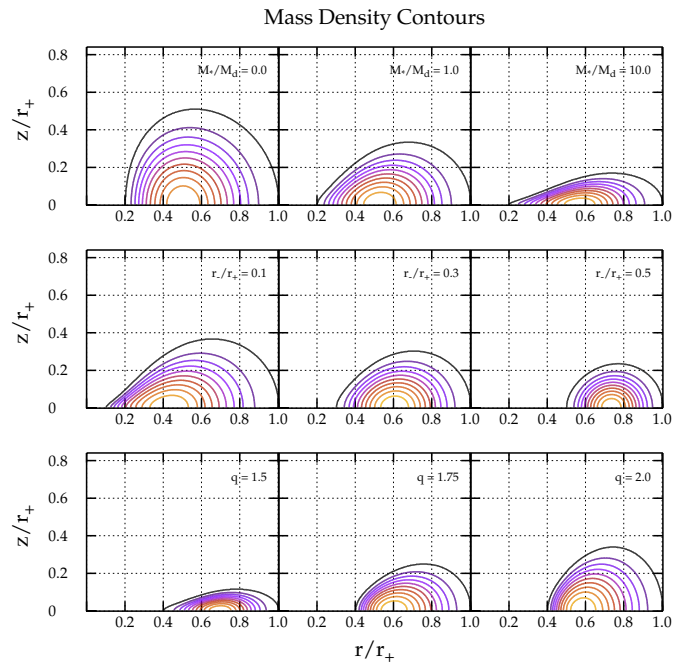


**Fig. 1** Top row: Mass density contours for models of varying values of  $M_*/M_d$  with  $q = 1.5$  and  $r_-/r_+ = 0.20$ . Contours trace ten divisions between the arbitrary low density of  $10^{-30}$  and the max density. Middle row: Contours for models with  $q = 1.5$  and  $M_*/M_d = 1$ , sweeping  $r_-/r_+$ . Bottom row: Contours for models with  $M_*/M_d = 25$  and  $r_-/r_+ = .4$ , sweeping  $q$ .

that systems which have  $Q \lesssim 1.5 - 1.7$  anywhere in the disk are unstable to nonaxisymmetric instability (*e.g.*, Durisen *et al.* 2007). For  $q = 2$ ,  $Q = 0$ . For  $q = 1.5$ , disks with small  $M_*/M_d$  show large regions where  $Q < 1.5 - 1.7$  while for large  $M_*/M_d$ ,  $q = 1.5$  disks show  $Q > 1.5 - 1.7$  everywhere. An additional effect of  $Q$  arises in regions where  $Q < 1$ . In such regions, traveling waves damp. For  $q \approx 2$ , the disk has  $Q \approx 0$  because  $\kappa^2 \approx 0$ . Qualitatively similar behavior between  $q = 1.5$  and  $1.75$  is seen. The region where  $Q < 1$  begins wide, decreases in width monotonically with increasing  $M_*/M_d$  and finally disappears. On grounds of the  $Q$  parameter, disks near  $q = 2$  are likely to be much more unstable than  $q = 1.5$  and  $1.75$  disks. For  $q = 1.5$  and  $1.75$ , systems with large  $M_*/M_d$  are likely to be stable based on  $Q$ .

Another parameter commonly used in the analysis of equilibrium disks is the ratio of the rotational kinetic energy to the absolute value of the gravitational potential energy,  $T/|W|$ .  $T/|W|$  is particularly useful in the analysis of gravito-rotation driven nonaxisymmetric modes in star-like objects.  $q = 1.5$  disks, Kepler-like disks, show higher values of  $T/|W|$  for large  $M_*/M_d$  than do  $q = 2$  disks.  $T/|W| \rightarrow 0.5$  for the largest  $M_*/M_d$  and  $r_-/r_+$  for all  $q$  and varying  $q$  and  $r_-/r_+$  has little effect on  $T/|W|$  for large  $M_*/M_d$ .  $T/|W|$  also varies differently across parameter space for different  $q$  making it less useful as a universal stability indicator for star/disk systems than has been found for toroids (Hadley & Imamura 2011) and *spheroidal* objects (*e.g.*, Tassoul 1978).

Two local measures of the importance of self-gravity,

$$p^2 = \frac{4\pi G \rho_o}{\Omega_o^2}, \quad (15)$$

and

$$\eta = \frac{\Omega_k^2}{\Omega_o^2} \quad (16)$$

are useful indicators of stability in thin-disks and ICTs (*e.g.*, Christodoulou & Narayan 1992, Andalib, Tohline, & Christodoulou 1997). Here,  $\Omega_k$  is the Keplerian angular velocity given by  $\Omega_k = \sqrt{GM_*/r_o^3}$ . Although  $p$  and  $\eta$  show different behavior and also vary with  $q$ , individually, each may be a useful indicator for the stability properties of thick, self-gravitating disk systems.

### 3 NONAXISYMMETRIC DISK INSTABILITIES

A foundation is presented for the understanding of non-axisymmetric disk modes, beginning with the linearized

evolution equations. This is followed by detailed descriptions of the character of the several types of modes observed (J, E/P, I,  $m=1$ ), followed by laying out, in  $(r_-/r_+, M_*/M_d)$  space for given  $q$ , the eigenvalues and character of the dominant low- $m$  modes. The section concludes with discussion and calculation of the angular momentum transport properties of representative modes from all classes, with particular attention to  $m = 1$ .

#### 3.1 Linearized Evolution Equations

Linearly unstable modes are found from solution of an Initial Value Problem (IVP) formulated from the hydrodynamics equations evaluated using Eulerian perturbations of the form,

$$A = A_o + \delta A(\varpi, z, t) e^{im\phi}, \quad (17)$$

where  $A_o$  is the equilibrium solution and  $\delta A$  is the perturbed amplitude in the meridional plane. For all complex perturbed quantities, the physical solution corresponds to the real part.

From the perturbations and the hydrodynamic equations, a set of linearized evolution equations is formed (Hadley & Imamura 2011). In cylindrical coordinates, the linearized hydrodynamic equations are

$$\begin{aligned} \partial_t \delta \rho &= -im\Omega \delta \rho - \rho_o \frac{\delta v_\varpi}{\varpi} - \delta v_\varpi \partial_\varpi \rho_o - \delta v_z \partial_z \rho_o \\ &\quad - \rho_o \left( \partial_\varpi \delta v_\varpi + \frac{im}{\varpi} \delta v_\phi + \partial_z \delta v_z \right) \end{aligned} \quad (18)$$

$$\begin{aligned} \partial_t \delta v_\varpi &= -im\Omega \delta v_\varpi + 2\Omega \delta v_\phi - \frac{\gamma P_o}{\rho_o^2} \partial_\varpi \delta \rho \\ &\quad - (\gamma - 2) \frac{\delta \rho}{\rho_o^2} \partial_\varpi P_o - \partial_\varpi \delta \Phi_g, \end{aligned} \quad (19)$$

$$\begin{aligned} \partial_t \delta v_\phi &= -im\Omega \frac{\delta v_\varpi}{\varpi} \partial_\varpi (\Omega \varpi^2) - \frac{im}{\varpi} \frac{\gamma P_o}{\rho_o^2} \delta \rho \\ &\quad - \frac{im}{\varpi} \delta \Phi_g, \end{aligned} \quad (20)$$

$$\begin{aligned} \partial_t \delta v_z &= -im\Omega \delta v_z - \frac{\gamma P_o}{\rho_o^2} \partial_z \delta \rho - (\gamma - 2) \frac{\delta \rho}{\rho_o^2} \partial_z P_o \\ &\quad - \partial_z \delta \Phi_g. \end{aligned} \quad (21)$$

The perturbed disk gravitational potential  $\delta \Phi_d$  is found by solving the linearized Poisson equation,

$$\nabla^2 (\delta \Phi_d e^{im\phi}) = 4\pi G \delta \rho e^{im\phi} \quad (22)$$

for the azimuthal mode  $m$  under consideration. The star follows a spiral trajectory giving rise to the *indirect potential*,

$$\delta \Phi_* = -\frac{GM_*}{r} \left( \frac{\delta_* \cdot \mathbf{r}}{r^2} \right) \quad (23)$$

where  $\delta_*$  is the perturbed location of the star. Both  $\delta\Phi_d$  and  $\delta\Phi_*$  are included in the evolution equations. We find  $\delta_*$  by solving the linearized stellar equation of motion,

$$\begin{aligned} \partial_{tt}\delta_* &= \pi G(\hat{\mathbf{x}} + i\hat{\mathbf{y}}) \int \frac{\delta\rho}{r^3} \varpi^2 d\varpi dz \\ &+ \pi G\delta_* \int \frac{\rho_o}{r^3} \left( 3\left(\frac{\varpi^2}{r^2}\right) - 2 \right) \varpi^2 d\varpi dz, \end{aligned} \quad (24)$$

simultaneously with the linearized evolution equations. The Cartesian coordinates of the star are related as  $\delta_{*,y} = i\delta_{*,x}$  so that the perturbed stellar potential is

$$\delta\Phi_* = -\frac{GM_*}{r} \left( \frac{\delta_{*,x}^R}{r^2} + i\frac{\delta_{*,x}^I}{r^2} \right) \varpi e^{i\phi} \quad (25)$$

where  $\delta_{*,x}^R$  and  $\delta_{*,x}^I$  are the real and imaginary parts of the perturbed  $\hat{x}$  component of the stellar position.

Equilibrium values for  $\rho$  and  $\mathbf{v}$  are used as the background for solution of the IVP equations. The IVP is evolved on the same grid as the equilibrium models. Spatial derivatives are given in finite difference form and time derivatives left continuous. The perturbed solutions are advanced in time using a fourth order Runge-Kutta method. The numerical code is described in detail in Hadley & Imamura (2011). We usually used grid sizes of  $n_\varpi \times n_z = 512 \times 512$  although for disks with large  $r_-/r_+$  and  $q = 1.5$ , we sometimes used grids of size  $1024 \times 1024$ . Convergence tests were run with resolutions of  $256^2$ ,  $512^2$  and  $1024^2$ , with eigenvalues typically agreeing with each other to within a few percent. Less agreement was found near transition regions, boundaries between mode types, which tended to shift slightly in  $r_-/r_+$  for a given  $M_*/M_d$ .

Boundary conditions consist of mirror symmetry about the equatorial plane. Perturbed velocities in the  $\varpi$  and  $z$  directions are set to zero on the surface of the disk, while the mass density perturbation is set to zero gradient. The gravitational potential is solved in the Coulomb gauge and computed at the outer grid boundaries using a sum over spherical harmonics up to  $l = 16$ .

We find that our results agree with the early-time behavior of full nonlinear simulations made using the CHYMER code (Hadley *et al.* 2014). In tests, we agreed with the work of Blaes (1985), who found analytic eigenvalues for infinitely slender  $q = 2$  non-self-gravitating tori within about 10%. The evolution equation coefficients at the disk outer boundary are weakly singular, and likely introduce some problems for our fixed grid code causing the discrepancy.

The evolution of the perturbed disk was followed by monitoring  $|\delta\rho|/\rho_o$  at three points in the disk midplane to ensure that instability is global in nature. A model is

deemed dynamically stable if it shows no global growth after 30 - 40  $\tau_o$  where  $\tau_o$  is the rotation period at the radius of the density maximum. We monitor growth until time dependence has settled into stable exponential behavior,

$$f(t) = f_0 e^{-i\omega_m t} \quad (26)$$

for any perturbed quantity  $f$ . We choose these and other sign conventions to be consistent with previous workers in the field (*e.g.*, see Kojima 1986). Growth rates and oscillation frequencies are determined from least squares fits to the logarithm of the amplitude and the phase, respectively. For our definition, the real part of  $\omega$  refers to the frequency of the perturbation while the imaginary part refers to the growth rate. Prograde modes have  $\mathcal{R}(\omega) < 0$ . For our choice of the form for the azimuthal eigenfunction, normalized eigenvalues are defined as

$$y_1(m) = -\left( \frac{\mathcal{R}(\omega_m)}{\Omega_o} + m \right) \quad \text{and} \quad y_2(m) = \frac{\mathcal{I}(\omega_m)}{\Omega_o}. \quad (27)$$

Here  $\mathcal{R}(z)$  and  $\mathcal{I}(z)$  take the real and imaginary parts of a complex variable.

The corotation radius,  $r_{co}$ , is where the pattern frequency of the mode equals the orbital frequency of the fluid. The co-rotation radius acts as a resonance point in the disk where periodic forcing may amplify the density perturbation (see Goldreich & Tremaine 1979). If there is no real component in the density perturbation, a singularity may arise at the corotation resonance point (see eq. 26-27). The  $y_1(m)$  are defined so that if  $y_1(m) < 0$ ,  $r_{co} > r_o$  and if  $y_1(m) > 0$ ,  $r_{co} < r_o$ . For power-law  $\Omega$ ,  $r_{co}$  is given by:

$$\frac{r_{co}}{r_o} = \left( \frac{y_1(m)}{m} + 1 \right)^{-1/q} \quad (28)$$

The inner and outer Lindblad resonances  $r_{ilr}$  and  $r_{olr}$ , are located where the real part of  $\omega_m$  equals  $\pm\kappa$ . For power-law  $\Omega$ ,  $r_{ilr}$  and  $r_{olr}$  are related to  $r_{co}$  by:

$$\frac{r_{lr}}{r_{co}} = \left( 1 \pm \frac{\sqrt{4-2q}}{m} \right)^{1/q} \quad (29)$$

The vortensity is defined as

$$\mathbf{\Lambda} = \frac{\nabla \times \mathbf{v}}{\Sigma} \quad (30)$$

where  $\Sigma$  is the column density. For axial disks that rotate on cylinders with power law angular velocity, the only nonzero component of  $\mathbf{\Lambda}$  is

$$\Lambda_z = (2-q) \left( \frac{\Omega}{\Sigma} \right). \quad (31)$$

Vortensity modes arise when corotation falls at extrema in  $\Lambda_z$  (Papaloizou & Savonije 1991).

For analysis purposes, we calculate the work done locally by the perturbed kinetic energy, and the perturbed enthalpy which also accounts for the perturbation in the acoustic energy (see Kojima 1989). The perturbed kinetic energy and acoustic energy are designated as  $E_k$  and  $E_h$ , respectively and, for a polytrope, are given by:

$$E_k = \frac{1}{2}\rho\langle\delta v_\varpi^2 + \delta v_\phi^2 + \delta v_z^2\rangle \quad (32)$$

$$E_h = \frac{1}{2}\gamma\frac{P}{\rho^2}\langle\delta\rho^2\rangle \quad (33)$$

Here, the brackets represent time-averaged perturbed quantities. The total energy of the mode is the sum of the two. The time rate of change of the perturbed energy may be broken down into the time rate of change of the stresses:

$$\partial_t\sigma_R = -\rho_o\varpi\partial_\varpi(\delta v_\phi\delta v_\varpi) \quad (34)$$

$$\partial_t\sigma_G = -\rho_o(\delta\mathbf{v}\cdot\nabla)(\delta\Phi_d + \delta\Phi_*) \quad (35)$$

$$\partial_t\sigma_h = -\nabla\cdot(\delta P\delta\mathbf{v}) \quad (36)$$

where  $\sigma_R$  is the Reynolds stress,  $\sigma_G$  is the gravitational stress, and  $\sigma_h$  is the acoustic stress.

### 3.2 Classification Of Nonaxisymmetric Disk Modes

Modes are identified from their morphological and dynamical properties. We use characteristics including the winding of their arms, the regions in the disk where they have the largest amplitude, locations of corotation and vortensity extrema, and the self-gravity parameter  $p$  to classify modes. We have also examined the ratio of gravitational and Reynolds stress rates integrated over the disk,

$$\mathcal{R} = \frac{\int\partial_t\sigma_G d^3x}{\int\partial_t\sigma_R d^3x} \quad (37)$$

and found that it tracks mode type almost exactly as  $p$  does for  $m \geq 2$ , confirming the relative importance of self-gravity.

No one characteristic is sufficient or necessary to define mode type. In the following subsections we present representative models that characterize each mode type. Tables 1 to 4 summarize the properties of the modes presented in the figures and discussed in

the following sections. The azimuthal mode numbers  $m$  with the highest growth rate in the amplitude of the density perturbation are illustrated and discussed in Sections 3.3 and 3.3.4. The reader may find it helpful to reference this section to understand which azimuthal mode number dominates respective modes (J, E/P, I,  $m=1$ ) discussed.

#### 3.2.1 J Modes

J modes, the Jeans-like modes, are driven by self-gravity. They dominate systems with narrow,  $r_-/r_+ > 0.30$ , and high mass disks,  $M_*/M_d < 0.2$ , where the self-gravity parameter  $p \gtrsim 7.5$ . For given  $M_*/M_d$ , J modes with successively higher  $m$  dominate as  $r_-/r_+$  increases (see Figs ??-??).

In Table 1, we outline the parameters of four representative star disk systems which exhibit J modes. The properties of typical J modes are illustrated in Figure 2. We show constant phase loci for  $\delta\rho/\rho_o$  and  $\mathcal{W}$ , amplitudes of  $\delta\rho/\rho_o$  and  $\mathcal{W}$  subject to an arbitrary scaling factor, work integrals, and stress rates in the disk midplane for  $q = 1.5$  disks with  $M_*/M_d = 0.01$  and large  $r_-/r_+$ . Here

$$\mathcal{W} = \gamma\frac{P_o}{\rho_o^2}\delta\rho + \delta\Phi \quad (38)$$

is an alternative eigenfunction formed from the sum of the perturbed enthalpy and perturbed gravitational potential (Papaloizou & Pringle 1984).  $\mathcal{W}$  is a more natural eigenfunction for disks than is  $\delta\rho$  (*e.g.*, Hadley & Imamura 2011). This is apparent in the location of corotation which more closely tracks minima in  $|\mathcal{W}|$  than minima in  $|\delta\rho|$ . The benefit of tracking the  $\mathcal{W}$  eigenfunction is consistent with the corotation singularity at threshold being removed by  $\mathcal{W} = 0$  rather than by  $\delta\rho = 0$ . This behavior is also clear for the  $m \geq 2$  I and J modes. Note that in Figure 2 and in the rest of the paper, the amplitudes of  $\delta\rho/\rho_o$  and  $\mathcal{W}$  are normalized using their respective maximum values in the disk midplane. We have included the ratios of the unnormalized maximum values for  $|\delta\rho/\rho_o| / |\mathcal{W}|$  in the figure captions.

J modes do not show large variation in their properties. Dominant azimuthal wavenumbers for these models are illustrated in Figure 10, Section 3.3. The constant phase loci for  $\delta\rho/\rho_o$  are barlike for  $r < r_o$ , and show trailing spiral arms that extend for  $\sim \pi/m$  radians for  $r > r_o$  (Figure 2, column 2). The arms shown by  $\mathcal{W}$  lead those of  $\delta\rho$  indicating that the gravitational perturbation leads the enthalpy perturbation. The work integrals (Figure 2, column 4) for the  $m = 2$  modes show two distinct peaks in  $E_h$ , the first peak larger

Table 1: Representative J Modes

	$r_-/r_+$	$r_+/r_o$	$r_o$	$\tau_o$	$J$	$m$	$y_1, y_2$	$r_{ilr}/r_o, r_{olr}/r_o$	$r_{co}/r_o$
J1	0.402	1.51	6.47	187	1.43	2	-0.344, 0.110	0.714, 1.49	1.13
J2a	0.600	1.27	14.8	560	2.49	2	0.0297, 0.840	... , 1.30	0.990
J2b	"	"	"	"	"	3	-0.0271, 1.57	0.768, 1.22	1.01
J2c	"	"	"	"	"	4	-0.0844, 1.85	0.837, 1.18	1.01

**Table 1** Examples of J modes and their properties, giving (left to right) the radial aspect ratio of the disk, the disk outer radius, radius of density max, characteristic rotation time at density maximum  $\tau_o$  in polytrope units, total angular momentum, azimuthal mode number  $m$ , oscillation frequencies and growth rates of perturbed density, the radii of the inner and outer Lindblad resonances and the corotation radius.

than the second.  $E_k$  has one peak which is much lower in amplitude than the  $E_h$  peaks, near the center of the disk for large  $r_-/r_+$  models and skewed toward the inner edge for models with small  $r_-/r_+$ . For the  $m = 3$  mode, the minimum between the peaks does not go to zero, and the  $m = 4$  mode has only one peak each for  $E_k$  and  $E_h$ , with the  $E_k$  at higher amplitude. As for the stress rates (Figure 2, column 3)  $\partial_t \sigma_h$  dominates near the inner edge with higher amplitude for the  $r_-/r_+ = 0.40$  model than for the  $r_-/r_+ = 0.60$  model. In the central part of the disk,  $\partial_t \sigma_G$  is positive while  $\partial_t \sigma_h$  is negative. For the  $m = 2$  mode, the amplitudes of  $\partial_t \sigma_G$  and  $\partial_t \sigma_h$  are roughly comparable, while for the  $m > 2$  mode, the amplitude of  $\partial_t \sigma_G$  is higher than that of  $\partial_t \sigma_h$ .  $\partial_t \sigma_R$  is positive, but significantly lower in amplitude than either  $\partial_t \sigma_G$  or  $\partial_t \sigma_h$ , and is skewed toward the inner edge in the  $r_-/r_+ = 0.60$  model. The stress rates for the  $m = 2, 3$  and 4 are similar to each other.

### 3.2.2 P & Edge Modes

P and edge modes are driven by coupling of inertial waves across corotation. For both, corotation and the minimum in  $|\mathcal{W}|$  sit at  $\sim r_o$ . P and edge modes are dominant in the region in  $(r_-/r_+, M_*/M_d)$ -space to the far right and below the J mode corner (see Figures 14 and 15). Dominant azimuthal wavenumbers for these models are illustrated in Figure 11, Section 3.3. We identify three characteristic behaviors. For given  $M_*/M_d$  and increasing  $r_-/r_+$ , P and edge modes show: (i) bars near the inner edge of the disk with short forward phase shifts at  $r_o$  which switch to long trailing arms outside  $r_o$ , sometimes winding around the disk repeatedly; (ii) a similar mode with central bars and short leading phase shifts but with short trailing arms outside  $r_o$ ; and (iii) another mode with smoothly winding leading spiral arms. The instabilities with large winding number are referred to as edge modes. Edge modes are associated with the low  $r_-/r_+$  and/or high  $M_*/M_d$ . The modes in (ii) and (iii) are associated with the humps shown in the NSG  $y_2$  plot discussed in §3.3.3.

The characteristic behavior of edge modes and P modes is illustrated in Figures 3 and 4 where a sequence of figures of  $m = 2$  modes for  $q = 2$ ,  $M_*/M_d = 10^2$ , and  $r_-/r_+ = 0.70$  to 0.10 systems are shown (see also Table 2). These models strongly resemble corresponding NSG disks. Threshold behavior between edge and P modes for NSG disks occurs at  $r_-/r_+ = 0.50$ , where models with  $r_-/r_+ < 0.50$  exhibit corotation radii slightly inside  $r_o$  and greater winding of the trailing arms, and models with  $r_-/r_+ > 0.50$  exhibit corotation radii slightly outside  $r_o$  and shorter trailing arms. For self-gravitating models, the threshold between edge and P modes is not as clearly defined. At transition, corotation moves across  $r_o$  but does not coincide with the extension of the arms. For example,  $r_{co} = 1.01r_o$  for the model at  $r_-/r_+ = 0.45$ , even though it has extended arms. The first forward phase shift falls near  $r_o$ , with a rapid switch to a trailing arm. As  $r_-/r_+$  decreases from 0.60,  $r_o$  moves further inside the geometric center of the disk, leaving more room for the trailing arm to extend. Note that there is a change in  $y_1$ , as seen in Figure 15 ( $y_1$  plotted for  $q = 2$ ,  $m = 2$ ,  $M_*/M_d$  vs.  $r_-/r_+$ ) in that models exhibiting P mode behavior have  $y_1 < 0$ , while edge modes have  $y_1 > 0$ . In edge modes, the number of wraps increases with decreasing  $r_-/r_+$ . The corresponding eigenfunctions in Figure 4 indicate that a second minimum appears when the trailing arm extends beyond the inner bar. For low  $r_-/r_+$ , the winding of the arms increases. The minima occur with more frequency toward the outer edge of the disk. The P mode work integral plot has two peaks in  $E_h$ , one lying close to the inner and one closer to the outer edge of the disk. As  $r_-/r_+$  decreases, a broad valley develops between them.  $E_k$  has a peak which lies inside the inner  $E_h$  peak, with a shoulder across the central region, going to zero at the outer edge of the disk. The edge mode work integral plot also has a narrow  $E_h$  peak near the inner edge which contains the peak in  $E_k$ , but both have very low amplitude except near the inner edge. The work integrals become oscillatory for smaller  $r_-/r_+$ . The stress plots show acoustic



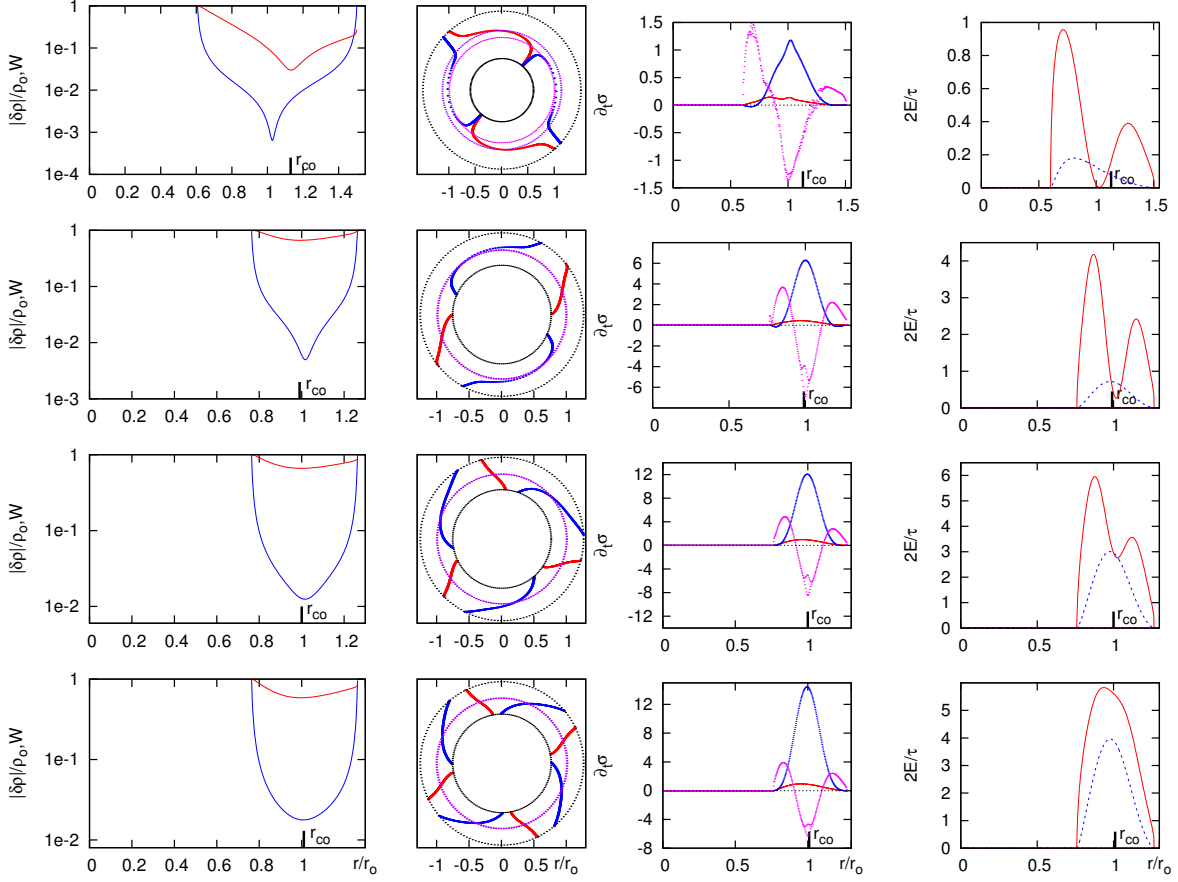


**Fig. 2**  $m = 2, 3,$  and  $4$  J modes for  $q = 1.5$  and  $M_*/M_d = 0.01$  systems with  $r_-/r_+ = 0.4$  and  $0.6$ , models J1, J2a, J2b, and J2c from top-to-bottom. We show  $\delta\rho$  and  $\mathcal{W}$  amplitudes and phases,  $\partial_t\sigma$ , and  $\delta J$ . For the eigenfunctions, the blue curve is for  $\delta\rho/\rho_0$  and the red curve for  $\mathcal{W}$ . For the  $\partial_t\sigma$ , the Reynolds stress is the red curve, the gravitational stress the blue curve, and the acoustic stress rate the magenta curve. For the perturbed energies, the kinetic energy is the blue curve and the enthalpy the red curve. For the first column, the ratios of the unnormalized maximum values for  $|\delta\rho|/|\mathcal{W}|$  are 2687, 9629, 4954 and 4256, respectively, from top-to-bottom.

Table 2: Representative P and Edge  $m = 2$  Modes

	$r_-/r_+$	$r_+/r_o$	$r_o$	$\tau_o$	$J$	$y_1, y_2$	$r_{co}/r_o$
P1	0.452	1.60	0.254	0.0808	5.05	-0.0649,0.0956	1.02
P2	0.500	1.49	0.403	0.161	6.35	-0.227,0.151	1.06
P3	0.600	1.33	1.09	0.712	10.4	-0.152,0.212	1.04
P4	0.700	1.21	3.37	3.88	18.4	-0.0736,0.126	1.02
E1	0.101	5.52	$6.13 \times 10^{-3}$	$3.03 \times 10^{-4}$	0.786	0.428,0.067	0.908
E2	0.202	2.99	0.0229	$2.18 \times 10^{-3}$	1.51	0.177,0.0833	0.959
E3	0.402	1.74	0.159	0.04	3.99	-0.0524,0.141	1.01

flux dominating near the inner and outer edges while Reynolds stress dominates the inner disk region, carrying opposite sign. Stress due to self-gravity is negligible for the P and edge modes.

### 3.2.3 $I^-$ & $I^+$ Modes

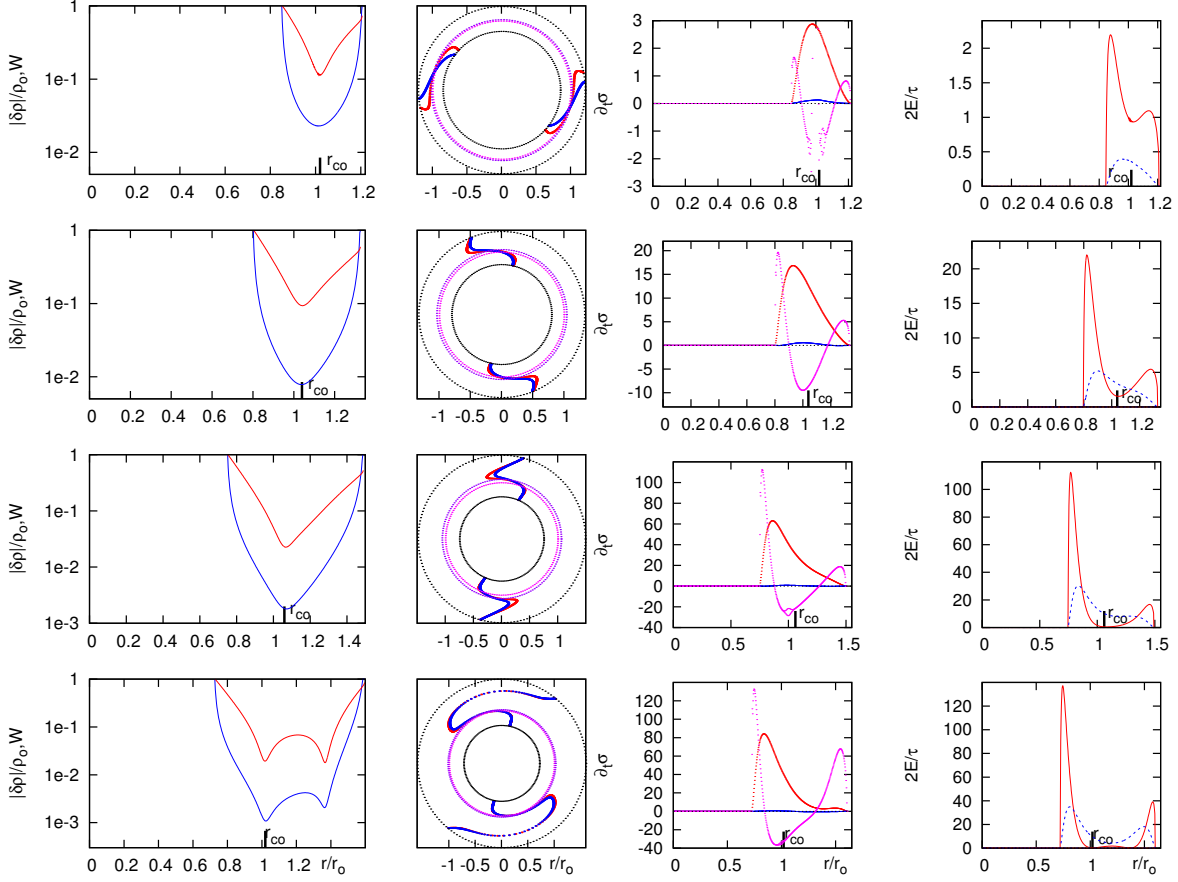
The I modes, modes with properties intermediate between those of the J and P modes were discovered by Goodman & Narayan (1986). There are two types of I modes, fast  $I^-$  modes with corotation inside  $r_o$ , sometimes inside  $r_-$ , and slow  $I^+$  modes with corotation outside  $r_o$ , sometimes outside  $r_+$ . Dominant azimuthal wavenumbers for I modes lie in parameter space illustrated in Figures 10 and 11, Section 3.3. The I mode region is seen in Figure 14 Section 3.3 as a wide arc extending to the right and below the J mode corner previously defined, ending in stable models curving from  $(r_-/r_+, M_*/M_d) = (0.70, 10.0)$  to  $(r_-/r_+, M_*/M_d) = (0.20, 0.01)$ . Equilibrium disks which show I modes consistently have  $p \lesssim 6 - 7.5$  and  $p \gtrsim 3$  for  $q = 2$  or  $\gtrsim 2$  for  $q = 1.5$ , both increasing with increasing  $m$ . Density contours are nearly concentric for small  $M_*/M_d$  disks, becoming somewhat flatter for high  $M_*/M_d$  disks. The threshold  $r_-/r_+$  above which the mode is type  $I^-$  roughly .5 for  $q = 1.5$ ,  $m = 2$  and is an increasing function of all of  $m$ ,  $q$  and  $M_*/M_d$  (see Figs ??-??, dashed lines).

Figure 5 depicts and Table 3 presents relevant properties for typical  $I^-$  modes. Corotation falls well inside  $r_o$ .  $|\mathcal{W}|$  shows a minimum near  $r_{co}$  while  $|\delta\rho/\rho_o|$  shows a minimum near  $r_o$ . The phase plots show a central bar and an outer bar connected by a trailing  $\pi/m$  phase shift in  $\delta\rho/\rho_o$  slightly outside  $r_o$ .  $\mathcal{W}$  is out of phase with  $\delta\rho/\rho_o$  at the inner edge, with a short leading arm that switches to trailing at  $r_{co}$ , coming into phase with  $\delta\rho/\rho_o$  at the outer edge. Models where  $M_*/M_d < 1$  exhibit bars near the inner and outer edges of the disk, while in higher  $M_*/M_d$  models, the bars become less perpendicular to the disk edges with  $\delta\rho/\rho_o$  and  $\mathcal{W}$  in phase and trailing at the outer edge. For the  $M_*/M_d = 5$  model pictured here,  $\delta\rho/\rho_o$  and  $\mathcal{W}$  come into phase

at  $r/r_o = 1.09$ . These trends are also seen in  $q = 1.75$  and 2, in that the  $M_*/M_d < 1$  models exhibit bars and the bars are less perpendicular in higher  $M_*/M_d$  models.  $\delta\rho/\rho_o$  amplitudes are similar to J modes, but the  $\mathcal{W}$  amplitudes of  $I^-$  modes typically have a dip near the inner edge of the disk. The work integrals for these models are similar in character to those of the J modes. The  $M_*/M_d = 5$  model shows stronger dominance of  $E_k$  in the disk, especially outside  $r_o$ . Stress plots are generally similar to those seen in the J modes.

$I^+$  modes are illustrated in Figure 6 and Table 3. Equilibrium density contours are nearly concentric for small  $M_*/M_d$  disks, becoming somewhat flatter for high  $M_*/M_d$  disks. Corotation falls outside  $r_+$  or, for model I5, just at  $r_+$ .  $|\mathcal{W}|$  does not show extrema when  $r_{co} > r_+$ .  $\mathcal{W}$  is in phase with  $\delta\rho/\rho_o$  near the inner edge of the disk, becoming out-of-phase for  $\varpi > r_o$ . There is roughly a  $\pi/m$  trailing phase shift in  $\delta\rho/\rho_o$  that lies close to  $r_o$ .  $q = 1.5$  models have bars near the inner and outer disk edges, becoming less perpendicular for higher  $M_*/M_d$ . The work integral of these models all show two peaks in  $E_h$  with the inner peak higher, and a region in the middle of the disk that is dominated by  $E_k$ . Unlike the  $I^-$  mode, where the peak in  $E_k$  lies at the zero between the two  $E_h$  peaks, the peak in  $E_k$  for the  $I^+$  mode lies within the region of the inner  $E_h$  peak. Notably, the  $q = 1.5$ ,  $r_-/r_o = 0.50$ ,  $M_*/M_d = 7$  model is dominated more strongly by  $E_k$  for much of the disk inside  $r_o$ . The stress plots show domination in the inner and outer regions by  $\partial_t\sigma_h$  while  $\partial_t\sigma_G$  dominates in the center of the disk. The Reynolds stress is positive with relatively low amplitude. The notable exception here is the  $q = 2$ ,  $r_-/r_o = 0.60$ ,  $M_*/M_d = 7$  model, which has a region inside  $r_o$  that is dominated by the Reynolds stress.

There is a region of parameter space that lies between  $I^+$  modes and edge modes where the characteristics of the models resemble neither. Unlike I modes, corotation lies near  $r_o$  and unlike edge modes, the  $\mathcal{W}$  phase lies significantly away from that of  $\delta\rho/\rho_o$ , indicating that self-gravity is important. There is a large variance in appearance of the models, with no strong characteristic identifying modes in this region.



**Fig. 3** Barlike P modes,  $m = 2$ , for disks with  $q = 2$  and  $M_*/M_d = 10^2$  for  $r_-/r_+ > 0.45$ , models P4, P3, P2, and P1 from top-to-bottom. We show  $\delta\rho$  and  $\mathcal{W}$  amplitudes and phases,  $\partial_t\sigma$ , and  $\delta J$ . For the eigenfunctions, the blue curve is for  $\delta\rho/\rho_0$  and the red curve for  $\mathcal{W}$ . For the  $\partial_t\sigma$ , the Reynolds stress is the red curve, the gravitational stress the blue curve, and the acoustic stress the magenta curve. For the perturbed energies, the kinetic energy is the blue curve and the enthalpy the red curve. For the first column, the ratios of the unnormalized maximum values for  $|\delta\rho|/|\mathcal{W}| = 99.43, 17.70, 4.74$  and  $4.48$ , respectively, from top-to-bottom.

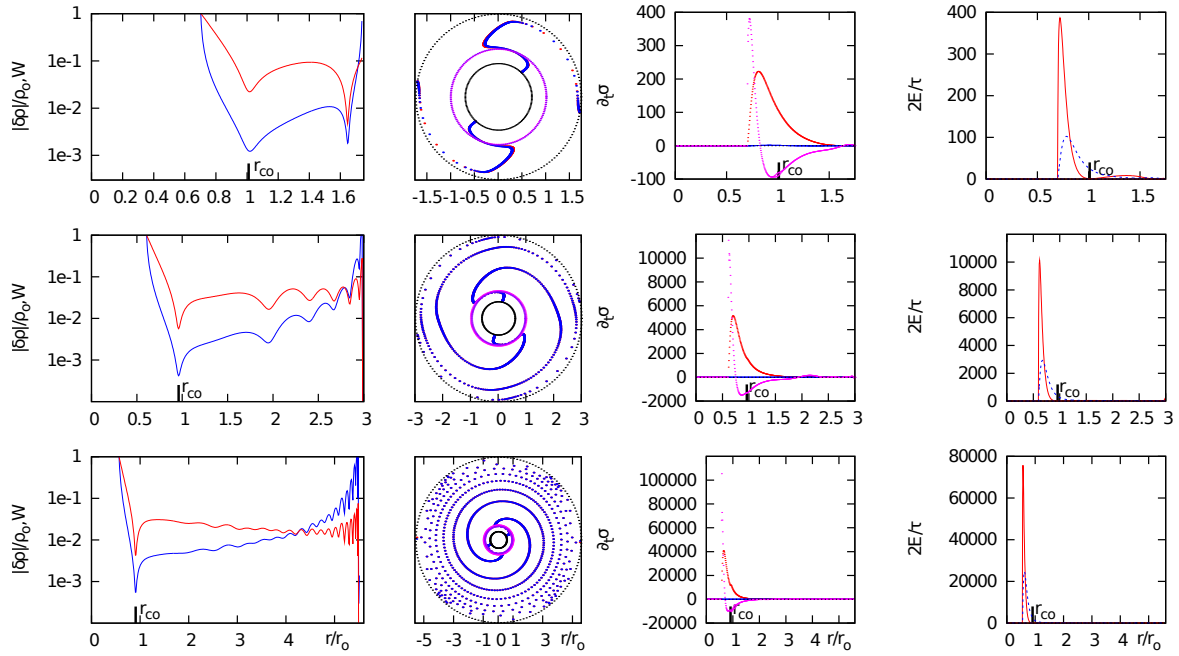


**Fig. 4** Barlike edge modes,  $m = 2$ , for disks with  $q = 2$  and  $M_*/M_d = 10^2$  for  $r_-/r_+ < 0.45$ , models E3, E2, and E1 from top-to-bottom. We show  $\delta\rho$  and  $\mathcal{W}$  amplitudes and phases,  $\partial_t\sigma$ , and  $\delta J$ . For the eigenfunctions, the blue curve is for  $\delta\rho/\rho_0$  and the red curve for  $\mathcal{W}$ . For the  $\partial_t\sigma$ , the Reynolds stress is the red curve, the gravitational stress the blue curve, and the acoustic stress the magenta curve. For the perturbed energies, the kinetic energy is the blue curve and the enthalpy the red curve. For the first column, the ratios of the unnormalized maximum values for  $|\delta\rho|/|\mathcal{W}|$  are 0.32, 0.14 and 0.0093, respectively, from top-to-bottom.

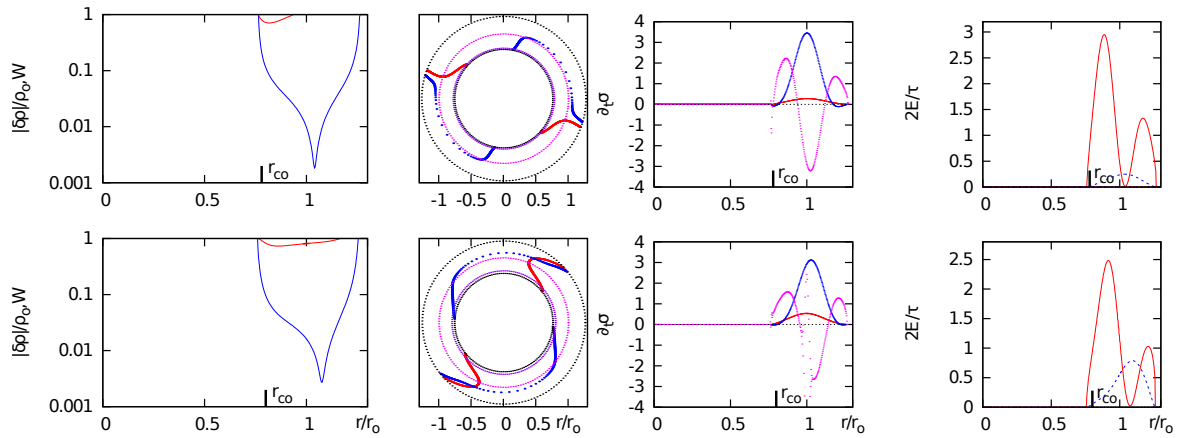


**Fig. 5** Barlike  $\Gamma^-$  modes,  $m = 2$  modes, with corotation inside  $r_0$  and sometimes inside  $r_-$  for disks with  $q = 1.5$  and  $M_*/M_d = 0.1$  and 5 for  $r_-/r_+ = 0.6$ , models I1 and I2 from top-to-bottom. We show eigenfunctions,  $\delta\rho$  and  $\mathcal{W}$  amplitudes and phases,  $\partial_t\sigma$ , and  $\delta J$ . For the eigenfunctions, the blue curve is for  $\delta\rho/\rho_0$  and the red curve for  $\mathcal{W}$ . For the  $\partial_t\sigma$ , the Reynolds stress is the red curve, the gravitational stress the blue curve, and the acoustic stress the magenta curve. For the perturbed energies, the kinetic energy is the blue curve and the enthalpy the red curve. For the first column, the ratios of the unnormalized maximum values for  $|\delta\rho|/|\mathcal{W}|$  are 7685 and 5221, respectively, from top-to-bottom.

Table 3: Representative  $I^-$  and  $I^+$   $m = 2$  Modes

	$M_*/M_d$	$q$	$r_-/r_+$	$r_+/r_o$	$r_o$	$\tau_o$	$J$	$y_1, y_2$	$r_{ilr}/r_o, r_{olr}/r_o$	$r_{co}/r_o$
I1	0.1	1.5	0.600	1.27	14.9	511	2.75	0.905, 0.504	$\dots$ , 1.02	0.780
I2	5	1.5	0.600	1.26	16.2	176	9.41	0.784, 0.432	$\dots$ , 1.05	0.802
I3	7	2	0.600	1.30	7.68	49.8	7.47	-0.747, 0.169	$\dots$	1.26
I4	0.2	1.5	0.402	1.50	6.60	152	1.84	-0.993, 0.601	0.996, $\dots$	$> r_+$
I5	7	1.5	0.500	1.36	11.6	91.6	9.32	-0.737, 0.274	0.856, $\dots$	1.36

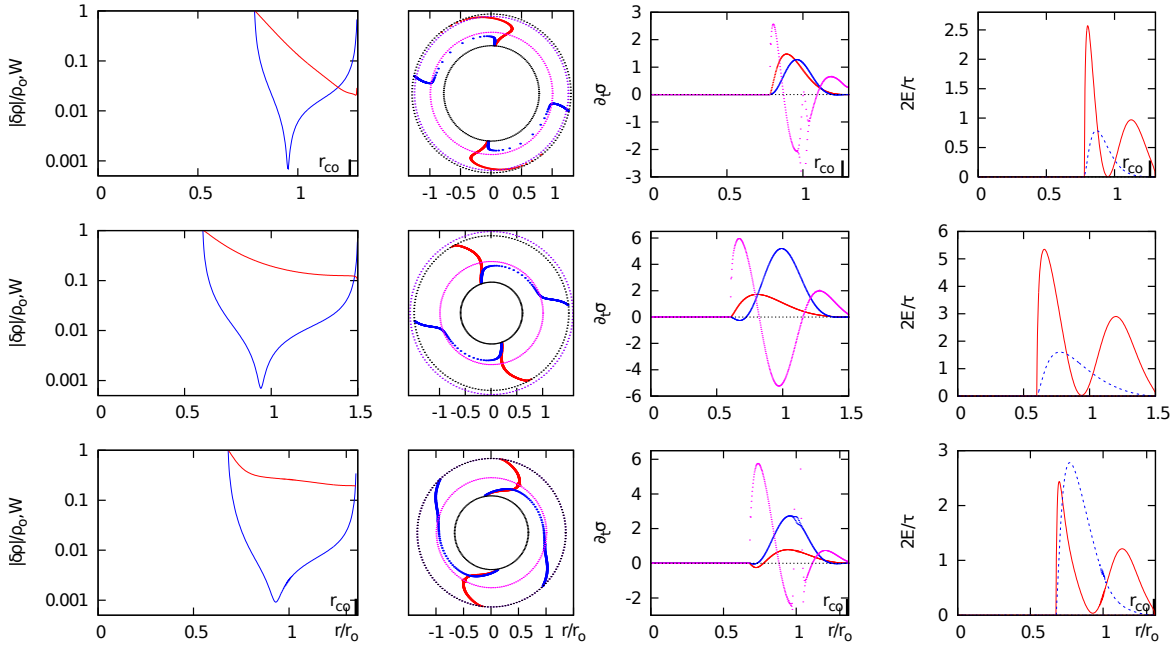


**Fig. 6** Barlike  $I^+$  modes,  $m = 2$  modes, with corotation outside  $r_o$  and sometimes outside  $r_+$  for disks with  $q = 2$ ,  $M_*/M_d = 7$ , and  $r_-/r_+ = 0.6$ , model I3,  $q = 1.5$ ,  $M_*/M_d = 0.2$ , and  $r_-/r_+ = 0.402$ , model I4, and  $q = 1.5$ ,  $M_*/M_d = 7$ , and  $r_-/r_+ = 0.5$ , model I5, from top-to-bottom. We show  $\delta\rho$  and  $W$  amplitudes and phases,  $\partial_t\sigma$ , and  $\delta J$ . For the eigenfunctions, the blue curve is for  $\delta\rho/\rho_o$  and the red curve for  $W$ . For the  $\partial_t\sigma$ , the Reynolds stress is the red curve, the gravitational stress the blue curve, and the acoustic stress the magenta curve. For the perturbed energies, the kinetic energy is the blue curve and the enthalpy the red curve. For the first column, the ratios of the unnormalized maximum values for  $|\delta\rho|/|W|$  are 634, 2082 and 3266, respectively, from top-to-bottom.

### 3.2.4 $m = 1$ Modes

Several kinds of  $m = 1$  modes have been found: (i) the eccentric instability discovered by Adams, Ruden, & Shu (1989 and named A modes by Woodward, Tohline, & Hachisu 1994) where the central star moves off the center of mass of the equilibrium disk in response to the nonaxisymmetric gravitational forcing arising from the perturbed disk. This leads to the indirect potential that couples the star to the disk at the outer Lindblad resonance; (ii) an instability where the central star moves in response to forcing from the perturbed non-axisymmetric gravitational potential of the disk, but the effects of the indirect potential are small and the mode is driven by super-reflection of waves at corotation (Noh, Vishniac, & Cochran 1992); (iii) P and edge-like modes which were discovered in NSG disks

but can also develop in self-gravitating disks (Kojima 1986, 1989, Noh, Vishniac, & Cochran 1992, Woodward, Tohline, & Hachisu 1994); (iv) modes in which the disk perturbation arranges itself so that its center-of-mass remains fixed at the origin and the star does not move (Hadley & Imamura 2011); and (v) elliptical instabilities which arise from noncircular streamlines in the equilibrium disk (Ryu & Goodman 1994). We modelled axisymmetric equilibrium disks and so did not consider elliptical instabilities. We do find examples of the other one-armed modes in our simulations.

Properties of  $m = 1$  modes are illustrated by cuts through  $(r_-/r_+, M_*/M_d)$  space. We first present results for  $q = 2$  disks with  $M_*/M_d = 1$ , and  $r_-/r_+$  ranging from 0.05 to 0.60, see Table 4 and Figure 7.  $m = 1$  modes are important in this study, since they dominate higher order  $m$  for small  $r_-/r_+$  in many cases.

Table 4: Representative  $m = 1$  Modes

	$M_*/M_d$	$q$	$r_-/r_+$	$r_+/r_o$	$r_o$	$\tau_o$	$J$	$y_1, y_2$	$\frac{r_{ilr}}{r_o}, \frac{r_{olr}}{r_o}$	$r_{co}/r_o$
O1	1	2	0.052	9.52	0.126	0.287	0.357	-0.418,0.0815	...	1.31
O2	1	2	0.101	4.89	0.327	1.18	0.576	-0.502,0.248	...	1.42
O3	1	2	0.201	2.60	1.02	6.39	1.04	-0.428,0.519	...	1.32
O4	1	2	0.301	1.91	2.21	19.5	1.57	-0.363,0.571	...	1.25
O5	1	2	0.402	1.59	4.14	48.3	2.23	-0.358,0.478	...	1.25
O6	1	2	0.600	1.28	12.5	239	4.13	-0.694,0.465	...	$> r_+$
O7	0	1.5	0.100	2.70	1.40	31.8	0.447	-0.859,0.0108	..., ...	$> r_+$
O8	0.01	1.5	0.100	2.68	1.42	30.9	0.470	-0.935,1.22	..., ...	$> r_+$
O9	0.1	1.5	0.100	2.60	1.54	26.7	0.647	-0.607,1.031	..., ...	1.86
O10	1	1.5	0.100	2.35	2.12	18.5	1.72	-0.311,0.341	..., 2.03	1.28
O11	5	1.5	0.100	2.12	3.06	14.9	4.36	-1.036,0.0451	..., ...	...
O12	0.01	1.8	0.100	3.03	1.07	23.3	0.329	-0.925,1.13	2.41, ...	$> r_+$
O13	0.1	1.8	0.100	3.20	0.974	15.1	0.428	-0.600,0.931	0.954,1.16	1.66
O14	0.5	1.8	0.100	3.85	0.669	4.77	0.663	-0.487,0.425	0.831,1.90	1.45
O15	1	1.8	0.100	4.31	0.486	2.12	0.803	-0.534,0.199	0.876,2.01	1.53
O16	100	2	0.700	1.21	3.37	389	18.4	-0.0420,0.115	...	1.02

For growth rate dependence on azimuthal mode number  $m$ , refer to Section 3.3. We find that  $q = 2$  disks do not show A modes. They do show unstable  $m = 1$  modes, however, when the indirect potential is suppressed,  $m = 1$  modes persist. They are similar to those found in the full simulations but have faster growth rates. This suggests that the  $m = 1$  modes for  $q = 2$  are not those studied by Adams, Ruden, & Shu (1989, see also Noh, Vishniac, & Cochran 1992, Woodward, Tohline, & Hachisu 1994). We see inner coherent bars which make rapid  $\pi$ -phase changes near  $r_{co}$  outside of which loosely wound trailing spiral arms form. These modes are likely associated with edge-like modes. The  $r_-/r_+ = 0.60$  sequence, disks with narrow nearly circular cross-sections, usually show loose spiral structure, with an arm that winds on the order of  $\pi$  or less sometimes with a small region near the outer edge of the disk where there is a phase change and a small trailing arm forms. The  $m = 1$  modes of  $q = 2$  sequences approach structures found in NSG disks.

Next consider  $q = 1.5$  systems. Plots in Figure 8 show  $m = 1$  eigenfunctions for  $r_-/r_+ = 0.101$  and star-to-disk mass ratios,  $0.0 < M_*/M_d \leq 5.0$ . The low star mass limit, the toroid limit, shows a split bar structure (Hadley & Imamura 2011). With no central star, the disk must conserve linear momentum itself. The addition of even a small star changes the nature of instability as shown by the  $M_*/M_d = 0.01$  model. The star's motion results in the formation of a barlike structure outside of which a leading spiral arm appears, similar in appearance to a P mode, but with  $y_1 = -0.935$ . The mode is slow and corotation falls outside the disk. These properties are consistent with an  $I^+$  mode al-

though the appearance of the phase plot does not resemble an I mode. For larger  $M_*/M_d$ , the oscillation frequency is higher and corotation moves into the disk. The disks also show outer Lindblad resonances. The phase plots also change in this region switching to structures composed of a trailing central bar-like region that abruptly turns to a leading spiral arm outside  $r_o$  later switching to an outer trailing arm. The trailing arm is initially short but grows in size as  $M_*/M_d$  is made larger, but it never winds more than  $\approx \pi/4$  in phase, even for the largest  $M_*/M_d$  disks. These modes bear strong resemblance to the P modes seen in  $q = 2$  NSG disks. For  $M_*/M_d = 5$ , the mode again changes character and forms a segmented bar which undergoes a  $\pi$  phase shift at  $r_o$ . The disturbance is slowly rotating in the retrograde sense with  $y_1 = -1.04$  and  $y_2 = 0.0451$ . A similar structure is found for the  $M_*/M_d = 25$  disk where  $(y_1, y_2) = (-0.976, 0.121)$ , but here the mode is prograde. The  $m = 1$  mode approaches a neutral point as  $M_*/M_d$  increases, consistent with the stability of  $q < \sqrt{3}$  NSG star/disk systems. These results depend on  $q$ . For  $r_-/r_+ = 0.05$  and  $M_*/M_d = 10$ ,  $m = 1$  modes are stable for disks with  $q = 1.6$  and  $1.7$ .

The existence of low-frequency, retrograde  $m = 1$  modes was first discovered by Kato (1983). Kato showed that thin, nearly Keplerian disks, although not unstable to nonaxisymmetric modes, supported neutral low frequency retrograde  $m = 1$  modes. Later works showed that prograde low-frequency  $m = 1$  modes also existed, although, similarly to Kato (1983), excitation mechanisms for the modes were not identified (Okazaki 1991, Ogilvie 2008, Papaloizou, Savonije, & Henrichs 1992). The  $m = 1$  modes in Keplerian disks have oscil-

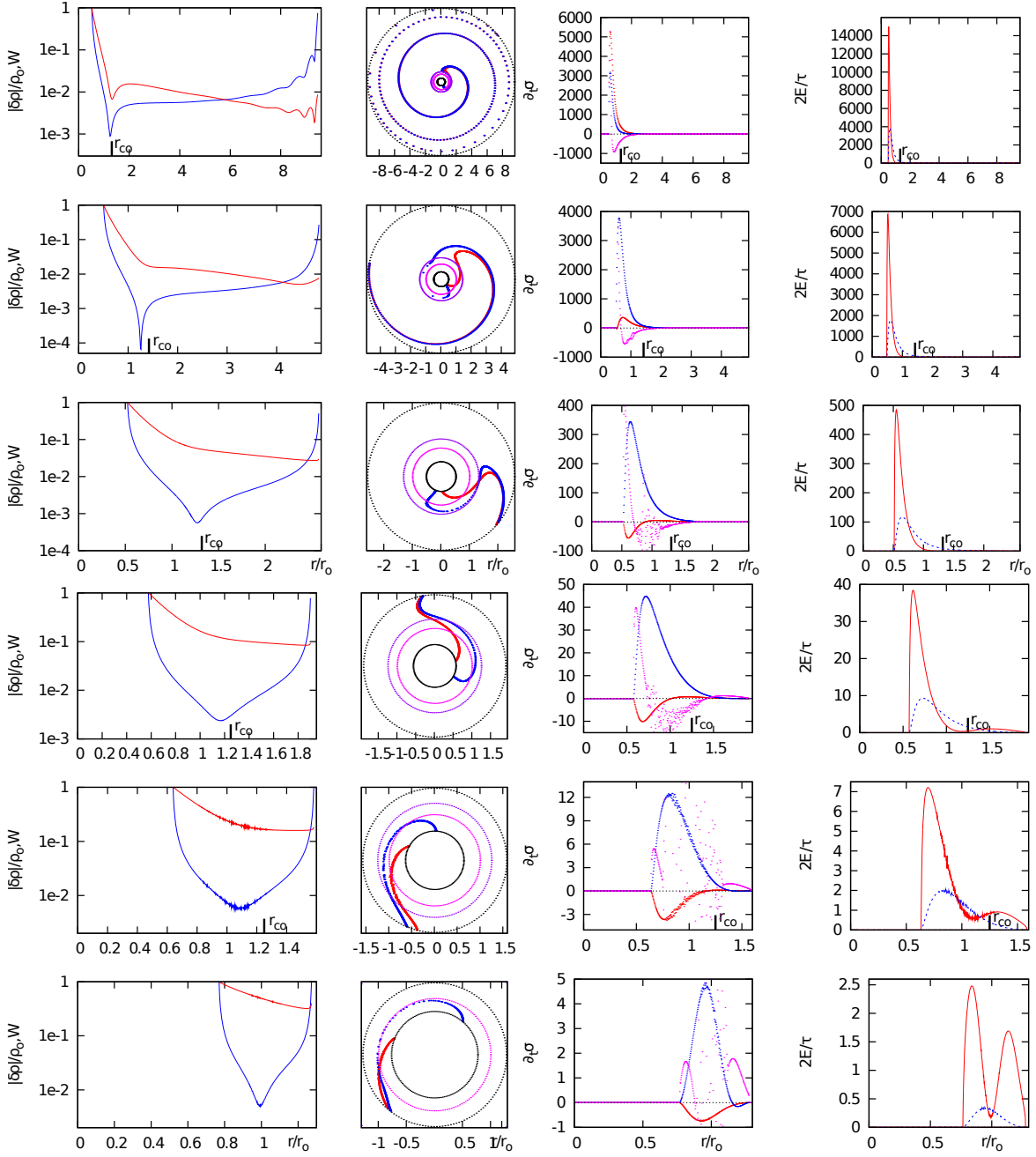


**Fig. 7**  $m = 1$  modes for models O1 to O6 from top-to-bottom. These are representative  $m = 1$  modes for  $q = 2$  disks with  $M_*/M_d = 1$ , and increasing  $r_-/r_+$ . We show  $\delta\rho$  and  $\mathcal{W}$  amplitudes and phases,  $\partial_t\sigma$ , and  $\delta J$ . For the eigenfunctions, the blue curve is for  $\delta\rho/\rho_0$  and the red curve for  $\mathcal{W}$ . For the  $\partial_t\sigma$ , the Reynolds stress is the red curve, the gravitational stress the blue curve, and the acoustic stress the magenta curve. For the perturbed energies, the kinetic energy is the blue curve and the enthalpy the red curve. For the first column, the ratios of the unnormalized maximum values for  $|\delta\rho|/|\mathcal{W}|$  are 1.54, 7.05, 46.68, 167.48, 431.38 and 3468, respectively, from top-to-bottom.

lation frequency given by  $\omega_1 \approx (c_s/\Omega r)^2 \Omega$  (Kato 1983). Using this result, we estimate the frequencies of our  $m = 1$  modes. Evaluating  $\omega_1$  at density maximum, we find  $\omega_1 \approx 0.072 \Omega_o$  where  $\rho_o = 3.67 \times 10^{-3}$ ,  $r_o = 6.56$ , and  $\Omega_o = 0.136$ . For the retrograde and prograde  $m = 1$  modes given above, our simulations yield oscillation frequencies  $-0.024 \Omega_o$  and  $0.039 \Omega_o$ , results smaller than, but similar to the estimated  $\omega_1$ .

We find A modes for  $q = 1.8$  disks. A sequence of  $q = 1.8$  disks for  $r_-/r_+ = 0.102$  is shown in Figure 9. The  $r_-/r_+$  place the models near the peak of the P mode hump and in the edge mode region. We see A mode behavior for the  $M_*/M_d = 0.5$  and 1 models when  $r_-/r_+ = 0.102$ , a smoothly winding trailing one-armed spiral. The development of the arm depends on the indirect potential. When the indirect potential is artificially suppressed, the  $m = 1$  mode is stable. Outside of the phase plot appearance, there is no strong marker for A modes.

### 3.3 Instability Regimes

Instability regimes for  $m = 1$  to 4 modes are laid out in  $(r_-/r_+, M_*/M_d)$  space. The results naturally break down into three mass realms,  $M_* \ll M_d$ ,  $M_* \approx M_d$ , and  $M_* \gg M_d$ . For our discussion, we present  $y_1$  and  $y_2$  for star/disk systems with  $M_*/M_d = 0$  to 100 and  $q = 1.5, 1.75$ , and 2 in Figures 10 to 12 and for  $q = 2$  disks in the  $M_* \gg M_d$  regime in Figure 13.

We did not fully examine  $m > 4$  modes in our current study. Of  $m = 1$  to 4, the fastest growing J mode is always  $m = 4$  where the J mode dominates; Presumably higher  $m$  J modes will be even more unstable until they should be cut off as the azimuthal wavelength approaches the azimuthal Jeans length. Outside of the Jeans dominated region, low modes are generally observed to have higher growth rates over larger spans of parameter space.

#### 3.3.1 $M_*/M_d \ll 1$

In the high disk mass regime, the  $M_*/M_d \ll 1$  regime, there is only weak dependence on  $q$ . To illustrate the disk mode properties, we show results for  $q = 1.5$  disks. Curves are given in Figure 10; Such modes are displayed by modes O7-O9 in Table 4 and form the left edge in the plots of Figure 14. Toroids illustrate nicely the properties of nonaxisymmetric modes in the high disk mass regime,  $M_*/M_d \ll 1$ .<sup>1</sup> Their growth rates,  $y_2$ ,

and oscillation frequencies,  $y_1$ , indicate the presence of I modes,  $m = 1$  I<sup>-</sup> and I<sup>+</sup> modes,  $m \geq 2$  I<sup>+</sup> modes, and  $m \geq 2$  J modes. Consider the  $m \geq 2$  modes first. For  $m \geq 2$ , toroids are stable for  $r_-/r_+ \lesssim 0.05$ . For  $r_-/r_+ \gtrsim 0.05$ , weak growth in  $m = 2$  is seen which peaks in strength around  $r_-/r_+ \sim 0.23$  where  $y_2 \sim 0.5$ , and then falls to zero near  $r_-/r_+ \sim 0.4$ . The mode has slow oscillation frequency,  $y_1 \sim -1$  so that corotation sits outside the location of density maximum,  $r_o$ . Hadley & Imamura (2011) classified these  $m = 2$  modes as I<sup>+</sup> modes. Around  $r_-/r_+ = 0.40$ , a second set of  $m \geq 2$  modes appears, modes with faster growth rates and faster oscillation frequencies. Near threshold, these  $m = 2$  modes have  $y_1 \sim -0.4$  which then slowly increases reaching  $y_1 \sim 0$  near  $r_-/r_+ \sim 0.7$ . This second set of modes has  $r_{co}$  nearly at  $r_o$ . Hadley & Imamura (2011) classified these fast modes as J modes. Toroid  $m = 1$  modes exhibit similar behavior but without showing J mode characteristics. For low  $r_-/r_+$ ,  $m = 1$  modes are weakly unstable with  $y_2 < 0.05$  near  $r_-/r_+ \sim 0.05$ . These  $m = 1$  modes are nearly stationary in the laboratory frame,  $y_1 \sim -1$ . Hadley & Imamura (2011) classified these slow  $m = 1$  modes as I<sup>+</sup> modes. Around  $r_-/r_+ \sim 0.3$ , a faster growing  $m = 1$  mode with faster oscillation frequency,  $y_1 \sim 1$ , appears. Corotation for these fast  $m = 1$  modes sits inside the inner radius of the disk leading to their classification as I<sup>-</sup> modes.

The extent to which toroids serve as the limiting case for high disk mass systems is shown by the  $M_*/M_d = 0.01$  system. The only difference seen for the  $m \geq 2$  modes is that the transition from the I<sup>+</sup> to J modes moves to slightly larger  $r_-/r_+$  when  $M_*/M_d = 0.01$ . Toroids are the limiting case for  $m \geq 2$  modes. For  $m = 1$  modes, however, qualitative differences arise. For the  $M_*/M_d = 0.01$  system,  $m = 1$  modes show faster growth rates than those shown by toroids and are the dominant mode for  $r_-/r_+$  up to 0.50-0.60. They are nearly stationary in the laboratory frame with  $y_1$  similar to, but smaller than those for the toroid  $m = 1$  modes. The  $y_1$  do not, however, show a jump as  $r_-/r_+$  increases. The  $y_1$  values remain close to -1 for all  $r_-/r_+$ . The presence of the star qualitatively alters the properties of  $m = 1$  modes even for this low  $M_*/M_d$  system. Similar results and conclusions are reached when the toroid results are compared to less massive disk systems, *e.g.*, the  $M_*/M_d = 0.1$  system.

#### 3.3.2 $M_*/M_d \approx 1$

For systems where  $M_d$  and  $M_*$  are comparable, the effects on the  $m = 1$  mode are larger because the gravitational potential of the star and disk have comparable strengths. These are exhibited by modes O1-O6 of Table 4 and Figure 7 as well as the middle region of figures

<sup>1</sup>Toroid results were discussed previously in Hadley & Imamura (2011). Here, we review results pertinent to the current discussion for the convenience of the reader.



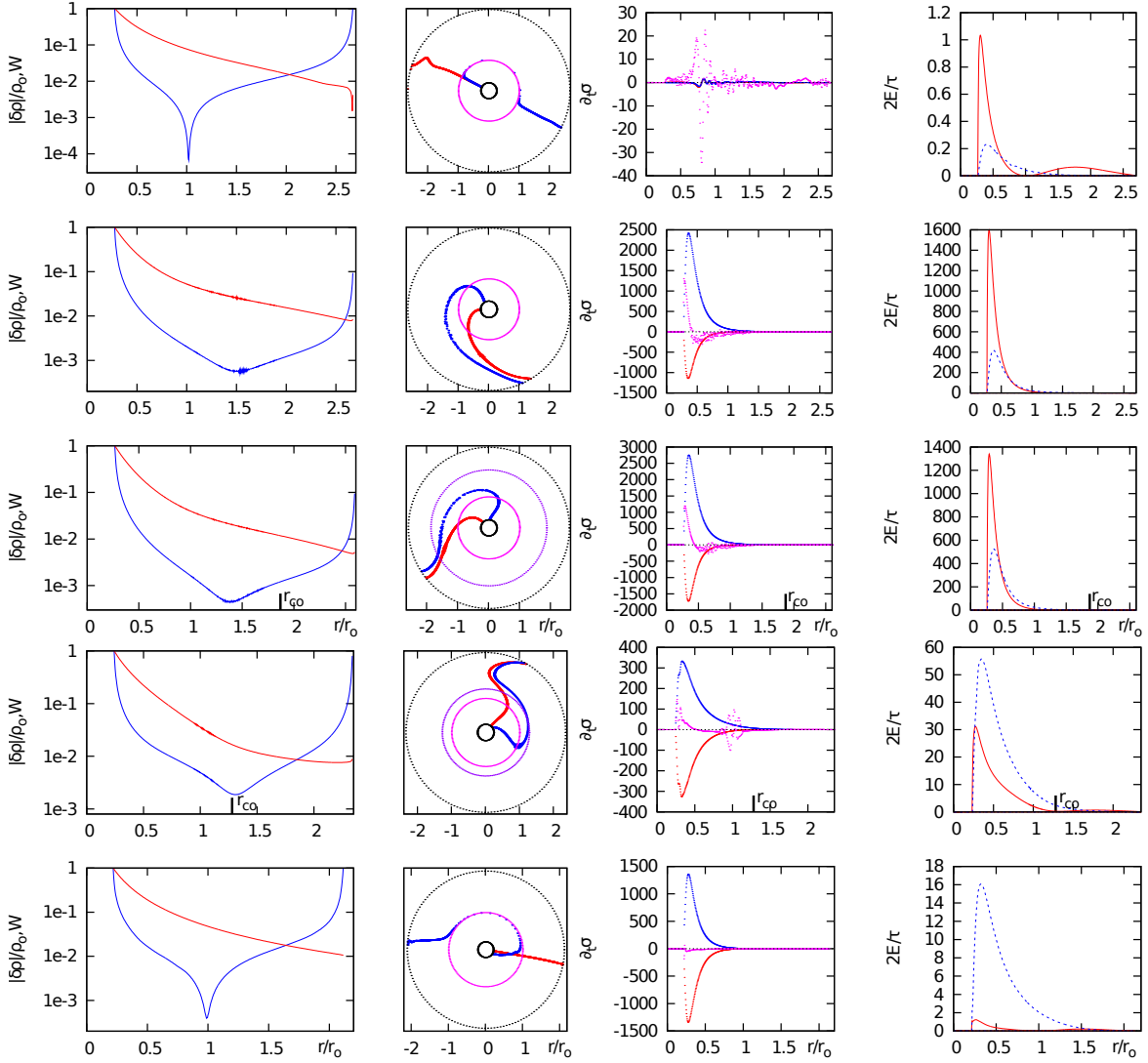


**Fig. 8**  $m = 1$  modes in Kepler-like disks with  $M_x/M_d = 0$  to 5 and  $r_-/r_+ = 0.101$ , models O7 to O11 from top-to-bottom. The bottom panel shows a slow retrograde mode nearly stationary in the laboratory frame. It strongly resembles the  $m = 1$  mode found in toroids (top panel). We show  $\delta\rho$  and  $\mathcal{W}$  amplitudes and phases,  $\partial_t\sigma$ , and  $\delta J$ . For the eigenfunctions, the blue curve is for  $\delta\rho/\rho_0$  and the red curve for  $\mathcal{W}$ . For the  $\partial_t\sigma$ , the Reynolds stress is the red curve, the gravitational stress the blue curve, and the acoustic stress the magenta curve. For the perturbed energies, the kinetic energy is the blue curve and the enthalpy the red curve. For the first column, the ratios of the unnormalized maximum values for  $|\delta\rho|/|\mathcal{W}|$  are 214.83, 172.63, 121.05, 28.12 and 6.61, respectively, from top-to-bottom.

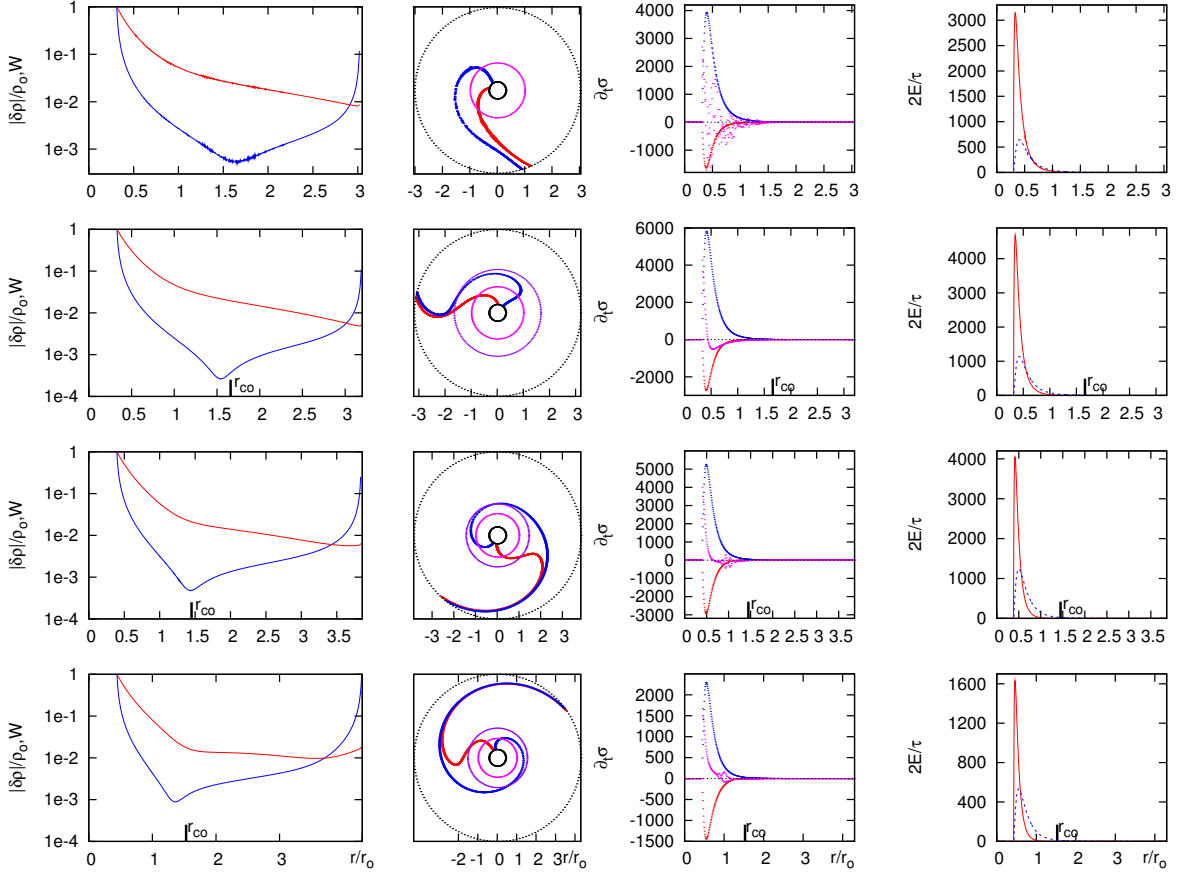


**Fig. 9**  $m = 1$  modes for disk models O12 to O15. The systems have  $q = 1.8$  and  $r_-/r_+ = 0.1$  for  $M_*/M_d = 0.01, 0.1, 0.5,$  and  $1$ , from bottom-to-top. The bottom two panels show  $m = 1$  A modes. We show  $\delta\rho$  and  $\mathcal{W}$  amplitudes and phases,  $\partial_t\sigma$ , and  $\delta J$ . For the eigenfunctions, the blue curve is for  $\delta\rho/\rho_\sigma$  and the red curve for  $\mathcal{W}$ . For the  $\partial_t\sigma$ , the Reynolds stress is the red curve, the gravitational stress the blue curve, and the acoustic stress the magenta curve. For the perturbed energies, the kinetic energy is the blue curve and the enthalpy the red curve. For the first column, the ratios of the unnormalized maximum values for  $|\delta\rho|/|\mathcal{W}|$  are 115.97, 71.61, 23.95 and 11.51, respectively, from top-to-bottom.

14 and 15. Although  $m = 1$  modes dominate low  $r_-/r_+$  disks, as they did for the  $M_*/M_d < 0.1$  disk systems, they show different character. The  $M_*/M_d \approx 1$  systems show two types of  $m = 1$  modes: (i) for  $q = 1.5$ , the oscillation frequency  $y_1$  shows a *humped* structure between  $r_-/r_+ = 0.05$  and 0.3-0.4 where it first rises from -0.5 to -0.25 and then returns to -0.5. The growth rate  $y_2$  rises from 0.25 to 0.4 and then falls to 0.3 over this range. Similar behavior is seen for the  $q = 1.75$  and 2 systems except that the upper end of the hump moves to larger  $r_-/r_+$  as  $q$  increases. (ii) For  $r_-/r_+ > 0.3-0.4$ , the character shown by the  $m = 1$  mode  $y_1$  and  $y_2$  is similar to that shown by the  $m = 1$  modes of the  $M_*/M_d = 0.01$  and 0.1 systems;  $y_2$  starts small and then slowly increases to  $\sim 0.4$ , and  $y_1$  smoothly falls from -0.5 to -1 as  $r_-/r_+$  increases. Both types of  $m = 1$  modes show  $r_{co}$  outside  $r_o$  and are classified as  $I^+$  modes.

The  $m \geq 2$  J modes also show strong changes as  $M_*/M_d$  increases but here it is because self-gravity weakens. Effects of weaker self-gravity are apparent by the  $M_*/M_d = 1$  systems. We find that: (i) the  $r_-/r_+$  where  $y_1$  makes the transition from  $\sim -1$  to 0, the change that marks the transition from  $I^+$  modes to J modes, moves to larger  $r_-/r_+$  as  $M_*/M_d$  increases for the  $m = 2$  modes. By the  $M_*/M_d = 1$  sequence, the transition has disappeared altogether. J modes are never dominant for systems where the star and disk masses are comparable. (ii) The slow  $m \geq 2$   $I^+$  modes become dominant starting around  $r_-/r_+ \sim 0.3-0.4$  giving way to  $m = 3$  and  $m = 4$   $I^+$  modes as  $r_-/r_+$  increases. Even though there is always only one dominant mode, all  $m \geq 2$  modes grow quickly and several modes may play roles in nonlinear simulations. (iii) At large  $r_-/r_+$ ,  $r_-/r_+ \gtrsim 0.6$ , a fast  $m = 2$   $I^-$  mode appears which dominates the disks. (iv) For  $q = 2$  disks, a fast  $m = 2$  mode also appears at small  $r_-/r_+$ . The mode is only weakly unstable and not expected to play a significant role in nonlinear simulations. These fast  $m = 2$  modes do not arise in  $q = 1.5$  and 1.75 disk systems. Overall, we find dependence on  $q$  but that the dependence is weak in systems where  $M_* \approx M_d$ .

### 3.3.3 $M_*/M_d \gg 1$

The character of instability changes and its dependence on  $q$  becomes stronger in the  $M_*/M_d \gg 1$  regime, the NSG disk regime. This is explored in Figures 12 and 11, with detailed plots for elements O11 and O16 of Table 4. These form the righthand side of Figures 14 and 15.

To explore these effects, we begin by showing  $y_1$  and  $y_2$  values for the  $m = 1$  and 2 modes of  $q = 2$  disks for disks with  $M_*/M_d = 10$  to  $10^3$  and for NSG

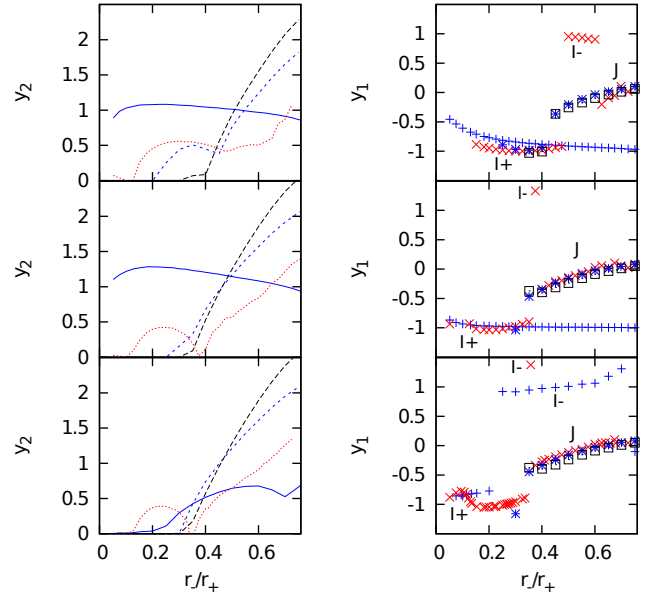


**Fig. 10** Oscillation frequencies,  $y_1$  and growth rates,  $y_2$ , for  $m = 1, 2, 3$ , and 4 modes for  $q = 1.5$ , high disk mass systems,  $M_*/M_d = 0.0, 0.01$ , and 0.1 from bottom-to-top. The  $m = 1$  modes are shown by blue solid lines and crosses,  $m = 2$  modes by red dotted lines and Xs,  $m = 3$  modes by blue dashed lines and asterisks, and  $m = 4$  modes by black long-dashed lines and boxes. Mode types are demarcated where clear identification could be made;  $m = 1$  modes generally follow their own scheme (see 3.2.4).

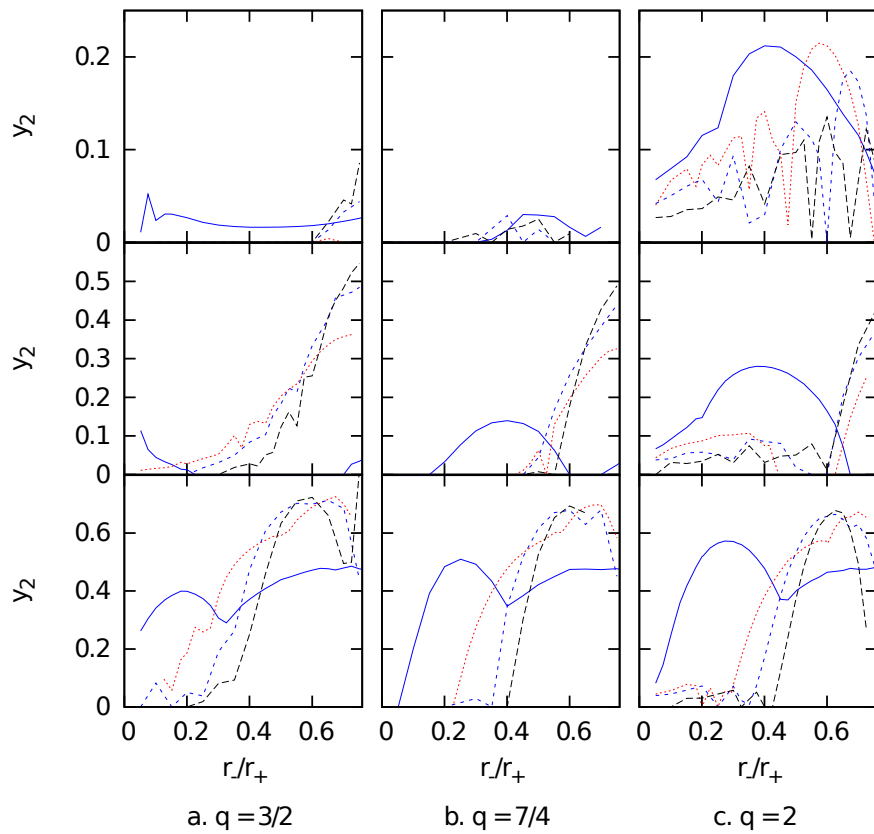


**Fig. 11** Growth rates,  $y_2$ , for the low  $m$  modes,  $m = 1, 2, 3$ , and  $4$  for systems with  $M_*/M_d = 1, 10$ , and  $100$  and  $q = 1.5, 1.75$ , and  $2$  disks. The columns are for  $q = 1.5, 1.75$ , and  $2$ , respectively. The rows are for  $M_*/M_d = 1, 10$ , and  $100$  from bottom-to-top. The  $m = 1$  modes are shown by blue solid lines,  $m = 2$  modes by red dotted lines,  $m = 3$  modes by blue dashed lines, and  $m = 4$  modes by black long-dashed lines.

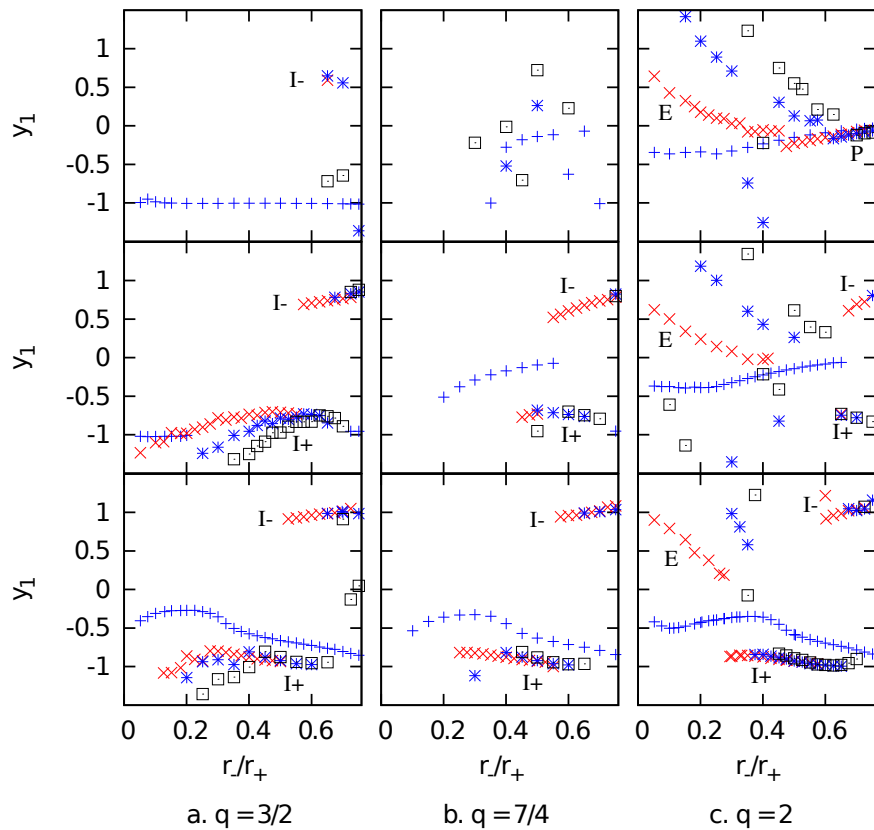


**Fig. 12** Oscillation frequencies,  $y_1$ , for the low  $m$  modes,  $m = 1, 2, 3$ , and  $4$  for systems with  $M_*/M_d = 1, 10$ , and  $100$  and  $q = 1.5, 1.75$ , and  $2$  disks. The columns are for  $q = 1.5, 1.75$ , and  $2$ , respectively. The rows are for  $M_*/M_d = 1, 10$ , and  $100$  from bottom-to-top. The  $m = 1$  modes are shown by blue crosses,  $m = 2$  modes by red Xs,  $m = 3$  modes by blue asterisks, and  $m = 4$  modes by black boxes. Mode types are demarcated where clear identification could be made;  $m = 1$  modes generally follow their own scheme (see 3.2.4).

disks in Figure 13. We first describe the NSG disk results. In the NSG limit,  $m = 1$  and 2 modes show two distinct behaviors. For small  $r_-/r_+$ , the modes are weakly unstable, with  $y_2 < 0.05$ , but have fast oscillation frequencies,  $y_1 \approx 1$  to 2 for both  $m = 1$  and 2. At higher  $r_-/r_+$ , a second type of mode appears, one with smaller oscillation frequency,  $y_1 \sim 0$ , and faster growth rate,  $y_2 > 0.14$ -0.15. The transition falls at  $r_-/r_+ \approx 0.28$  and 0.5 for the  $m = 1$  and 2 modes, respectively. The growth rate  $y_2$  grows, peaks at higher  $r_-/r_+$ , and then smoothly falls off approaching zero at large  $r_-/r_+$ . The peaks fall at  $r_-/r_+ = 0.55$  and 0.6 for  $m = 1$  and 2 modes, respectively. This behavior is shown by the other low- $m$  modes differing only in the  $r_-/r_+$  where the transition lies,  $r_-/r_+ = 0.62$  and 0.7 for  $m = 3$  and 4, respectively. Below the transitions, the instabilities are classified as edge modes. Above the transitions, they are classified as P modes (see §4.2).

The  $y_1$  and  $y_2$  values for the  $M_*/M_d > 100$  disks converge as  $M_*/M_d$  increases. Their dependence on  $r_-/r_+$  qualitatively follows that shown by NSG disk models for  $r_-/r_+ > 0.3$ ; NSG disks are not self-consistent below  $r_-/r_+ \sim 0.3$ . For  $m = 1$ , the first quantitative differences for systems with decreasing  $M_*/M_d$  appear in the  $M_*/M_d = 100$  sequence where the  $y_2$  fall below those of larger  $M_*/M_d$  sequences at  $r_-/r_+ > 0.7$ . Differences are noticeable for all  $r_-/r_+$  in the  $M_*/M_d = 10$  sequence where the peak growth rate,  $y_2 = 0.28$ , falls at  $r_-/r_+ \sim 0.40$  close to where peak falls for the higher  $M_*/M_d$  sequences but the growth rate is roughly twice as large. In line with this, the  $M_*/M_d = 1$  growth rate is about twice as large as for the  $M_*/M_d = 10$  model. For  $m = 2$  similar behavior is seen in that the sequences converge toward the NSG results as  $M_*/M_d$  increases but significant differences appear as early as the  $M_*/M_d = 500$  sequence for  $r_-/r_+ > 0.7$ .

For  $q = 1.75$  disks, the  $m = 1$  mode shows the high growth rate region, but the peak growth rate is smaller than for  $q = 2$  disks. The weak growth rate regime seen for  $q = 2$  disks does not appear in  $q = 1.75$  disks. For  $q = 1.5$  disks, the  $m = 1$  mode does not show the high growth rate regime, rather it shows only a weak growth rate region at  $r_-/r_+ < 0.15$ , where it has very small oscillation frequency,  $y_1 \sim -1$ . These slow  $m = 1$  modes are unstable for  $M_*/M_d \gtrsim 5$  to the NSG regime, with slow oscillation frequency,  $|\omega_1| \ll \Omega_0$  (Kato 1983) and may be retrograde or prograde depending on  $r_-/r_+$ . This behavior is not shown by  $q = 2$  systems. For higher  $m$  modes,  $y_1$  values decline as  $r_-/r_+$  increases with a transition to higher values for  $m = 2$  at  $r_-/r_+ = 0.70$ . The  $m = 2, 3$ , and 4 modes are unstable for  $r_-/r_+ > 0.5$  for the  $q = 1.75$  models. The  $m = 2$  mode dominates  $q = 1.5$  models for  $r_-/r_+ \sim 0.10$  to 0.60 and the  $m = 3$  and 4 modes dominate for  $r_-/r_+ \geq 0.65$ .

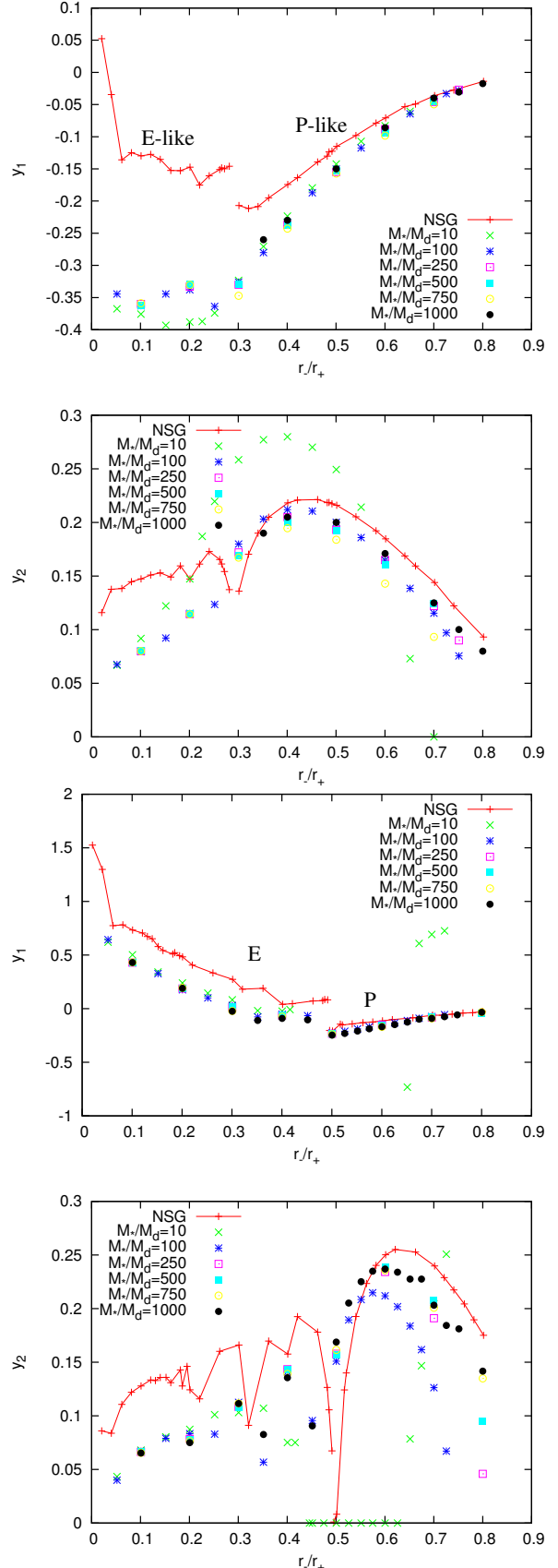


**Fig. 13** Comparison of the eigenvalues  $y_1$  and  $y_2$  for the (a)  $m = 1$  mode (left column), and (b)  $m = 2$  mode (right column) for  $q = 2$  NSG disks, and  $M_*/M_d = 10, 100, 250, 500, 750$ , and  $10^3$  disk systems.

### 3.3.4 Summary of Eigenvalue Results

Our results are highlighted in Figure 14 where we show  $y_1$  and  $y_2$  values as well as equilibrium parameters  $\eta$  and  $p$  for  $q = 1.5$  disks, and in Figure 15 where we do the same for  $q = 2$  disks. Our results are summarized in Figures 16 to 18 where we show the dominant modes for  $q = 1.5, 1.75,$  and  $2$  disks. Star/disk systems are generally unstable. For  $q = 2$  disks, which have a Toomre  $Q$  parameter of zero,  $m = 1$  modes usually dominate. Multi-armed modes,  $m \geq 2$ , are only dominant at large  $r_-/r_+$ , with some exceptions. Similar behavior is seen in the  $q = 1.75$  and  $1.5$  disks except that the range over which multi-armed modes dominate covers more of parameter space. For  $q = 1.5$  disks, the region stretches from high  $r_-/r_+$  to  $r_-/r_+ \sim 0.1$  for systems with moderate to low disk mass,  $M_*/M_d \approx 1$  to  $20$ . Protostellar and protoplanetary disks are expected to show nearly *Keplerian* rotation with  $M_*/M_d \approx 1$  to  $20$  and are thus expected to be dominated by  $m = 2, 3,$  and  $4$  modes. If they, however, are closer to constant specific angular momentum disks,  $q = 2$  disks, they are then expected to be dominated by  $m = 1$  modes.

The instability regimes for multi-armed modes in  $(r_-/r_+, M_*/M_d)$  space track the strength of self-gravitational effects as measured by the parameter  $p$  (independent of  $q$ ). In Figures 14 and 15, mode type boundaries have been overlaid on  $p$  which clearly show this. The most unstable are the J modes in the upper left hand corner, where  $p$  is largest.

Moving away from this corner we encounter I modes. At  $m = 2$  they are present for  $r_-/r_+ \geq 0.30$  and  $M_*/M_d \leq 10$ , excluding the J mode region itself. At lower  $r_-$  we observe  $I^+$  modes with corotation outside density max. At higher  $r_-/r_+$  we observe  $I^-$  modes with corotation well inside density max.

A stable region with  $y_2 \sim 0$  exists between  $I^-$  and the J modes, in a short arc sweeping from  $r_-/r_+ \approx 0.425$ ,  $M_*/M_d = 0.01$  to  $r_-/r_+ \approx 0.475$ ,  $M_*/M_d = 0.05$ . A second long arc of stability sweeps through parameter space from  $0.1 \leq r_-/r_+ \leq 0.20$ ,  $0.01 \leq M_*/M_d \leq 0.1$  to  $r_-/r_+ \approx 0.70$ ,  $17.5 \leq M_*/M_d = 50$ . The two arcs roughly follow  $p \approx 7.5$  and  $3$ . In the  $y_1$  plots in Figures 14 and 15 we see that these stable regions are where the dominant mode type changes. Sometimes, as in the transition from J to  $I^+$ , there is no “forbidden region” and the transition is marked by more subtle changes in the growth rates.

For one-armed spirals,  $m = 1$  modes, the instability regimes more closely follow the constant  $\eta$  curves than constant  $p$  curves. One-armed spirals are more unstable at large  $\eta$  than small  $\eta$ . For  $q = 2$  disks, a tongue of weak instability extends from intermediate  $M_*/M_d$  to

high  $M_*/M_d$  at intermediate  $r_-/r_+$ . This feature is not prominent in  $q = 1.5$  disks and is somewhat present in  $q = 1.75$  disks. Outside of this feature, the instability regimes for the  $m = 1$  modes are similar for  $q = 1.5, 1.75,$  and  $2$  disks. This does not mean the same types of  $m = 1$  modes populate the regions, however. For  $q = 1.5$  disks,  $m = 1$  modes are slow for small  $M_*/M_d$  and nearly stationary for large  $M_*/M_d$ . For  $q = 2$  disks,  $m = 1$  modes are also slow for small  $M_*/M_d$ , but show faster modes, modes with corotation near  $r_o$  and just outside  $r_o$  at large  $M_*/M_d$ . For Keplerian disks,  $q = 1.5$  disks,  $m = 1$  modes show  $r_{co}$  just outside  $r_o$  for systems with small  $r_-/r_+$  and  $M_*/M_d \approx 0.5-3$ .

We show the growth rates,  $y_2$ , as functions of  $M_*/M_d$  for  $r_-/r_+ = 0.1, 0.2, 0.3, 0.4, 0.5$  and  $0.6$  in Figure 19. For  $r_-/r_+ = 0.1$ , we see that  $m = 1$  dominates models with  $M_*/M_d < 10$  and shows comparable growth rates for high  $M_*/M_d$  models. As  $r_-/r_+$  increases, higher order  $m$  modes increase their growth rates, overtaking  $m = 1$  modes at  $r_-/r_+ = 0.5$  and  $0.6$ . At high  $r_-/r_+$ , we see the growth rates cascading upward in  $m$  for small  $M_*/M_d$ .

### 3.4 Angular Momentum Transport

The spiral arms in nonaxisymmetric disk modes exhibit both leading and trailing nature. This suggests that gravitational torques resulting from disk instabilities can manifest themselves through transport of angular momentum inward and outward through disks. Disks dominated by I and P modes show Reynolds stress torques which can dominate gravitational torques. For these cases, angular momentum transport is not determined by whether the gravitational perturbation leads or lags the density perturbations. Locally defined transport is expected. Here, we analyze torques for selected disk models. Transport is studied in the quasi-linear (QL) approximation using a model developed from the equation of conservation of angular momentum in its conservative form (*e.g.*, Shariff 2009).

We form the torque density,

$$\mathbf{N} = \mathbf{r} \times \mathbf{f} \quad (39)$$

where  $\mathbf{f}$ , the force density is given by

$$\mathbf{f} = \partial_t(\rho\mathbf{v}) = -\nabla \cdot \mathbf{S}. \quad (40)$$

In  $\mathbf{f}$ ,  $\mathbf{S}$  is the stress tensor which has the form

$$\mathbf{S} = \rho\mathbf{v}\mathbf{v} + \mathcal{P} + \frac{1}{4\pi G} \left( \nabla\Phi_g\nabla\Phi_g - \frac{1}{2}I\nabla\Phi_g \cdot \nabla\Phi_g \right), \quad (41)$$

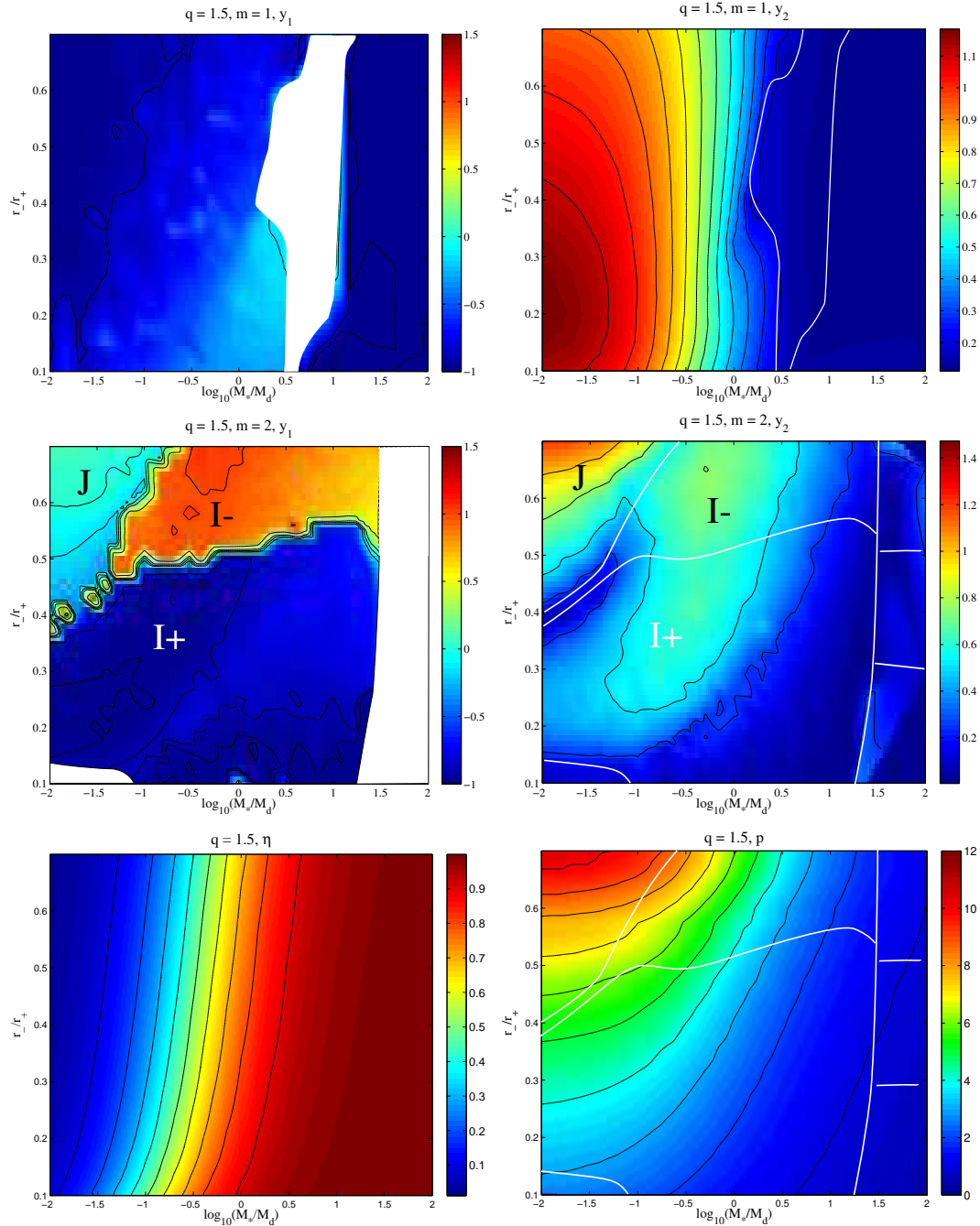


**Fig. 14** Oscillation ( $y_1$ ) and growth rate ( $y_2$ ) eigenvalues,  $\eta$  and  $p$  for  $q = 1.5$  disks.  $\eta$  contours step by .1,  $p$  contours step by 1 (smallest  $p \approx .5$ ). Regions without a resolved pattern frequency are whited out. For  $m = 2$  at  $M_*/M_d > 30$ , the boxed regions extrapolate stable,  $I^+$  and  $I^-$  modes, bottom to top, based on 0, 3 and 3 unstable models respectively.



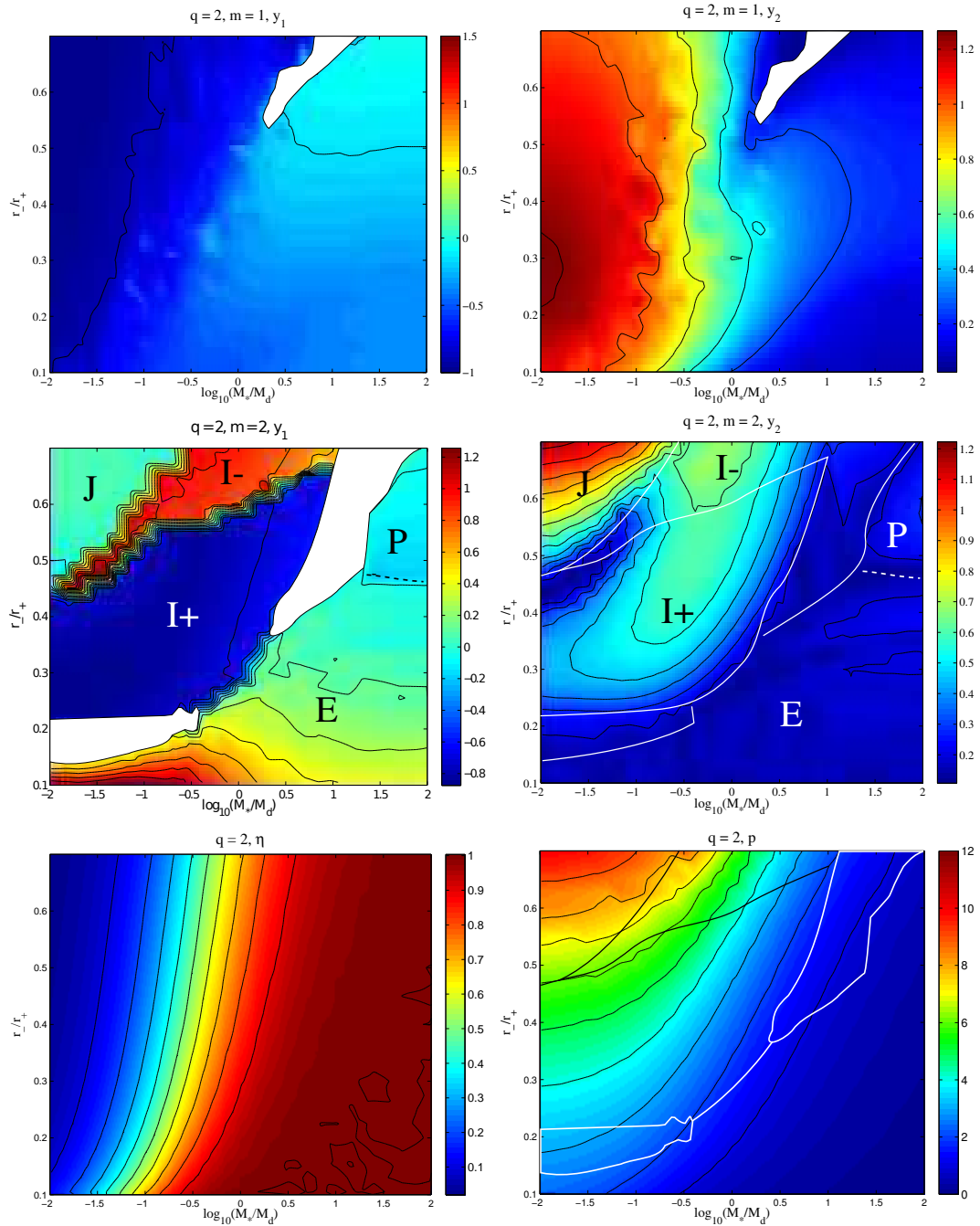


**Fig. 15** Oscillation ( $y_1$ ) and growth rate ( $y_2$ ) eigenvalues,  $\eta$  and  $p$  for  $q=2$  disks.  $\eta$  contours step by .1,  $p$  contours step by 1 (smallest  $p \approx .05$ ). Regions without a resolved pattern frequency are whited out.

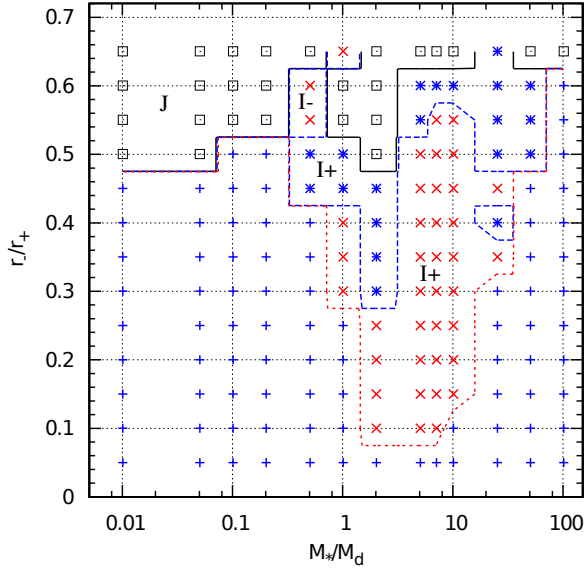


**Fig. 16** Dominant modes in  $(r_-/r_+, M_*/M_d)$  space for  $q = 1.5$  disks. The modes are denoted as follows:  $m = 1$  blue crosses,  $m = 2$  red Xs,  $m = 3$  blue asterisks, and  $m = 4$  black squares. Stable models are filled black squares. Note that the large  $m = 2$   $I^+$  region showed numerical difficulties with  $m = 1$  at  $q = 1.5$ , and  $m = 1$  may in fact dominate here.

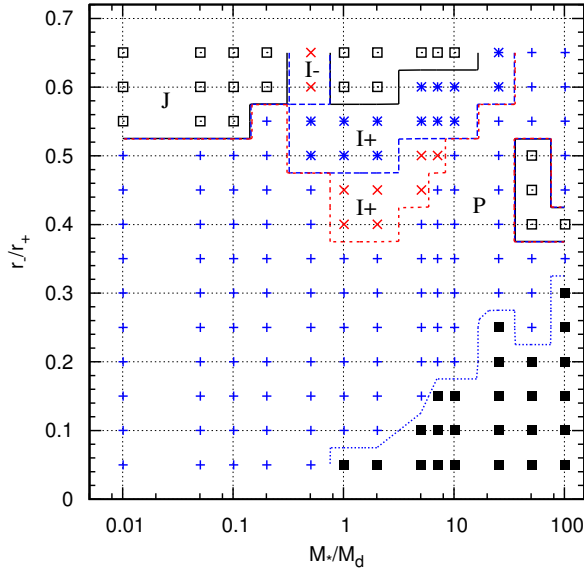


**Fig. 17** Dominant modes in  $(r_-/r_+, M_*/M_d)$  space for  $q = 1.75$  disks. The modes are denoted as follows:  $m = 1$  blue crosses,  $m = 2$  red Xs,  $m = 3$  blue asterisks, and  $m = 4$  black squares. Stable models are filled black squares.

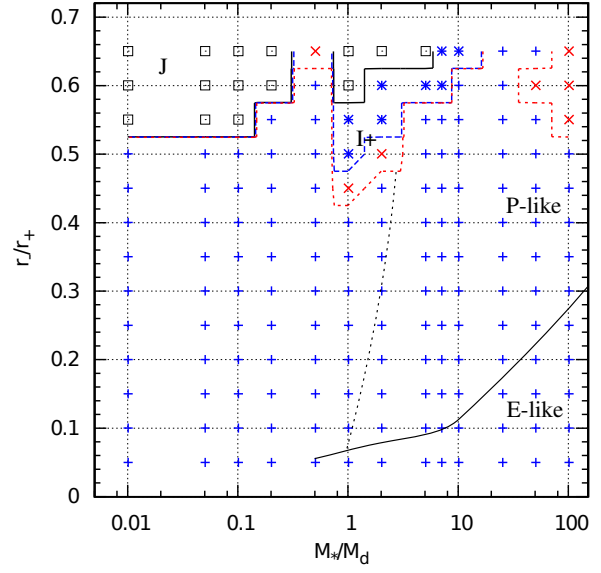


**Fig. 18** Dominant modes in  $(r_-/r_+, M_*/M_d)$  space for  $q = 2$  disks. The modes are denoted as follows:  $m = 1$  blue crosses,  $m = 2$  red Xs,  $m = 3$  blue asterisks, and  $m = 4$  black squares. Stable models are filled black squares.

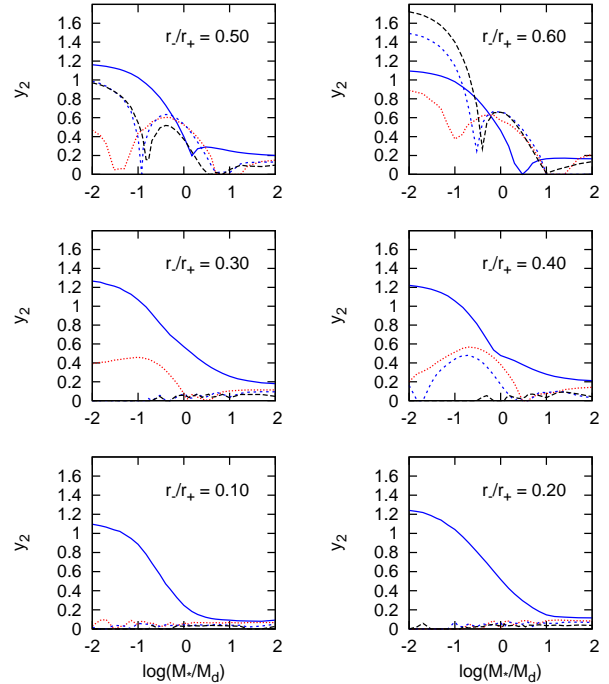


**Fig. 19** Growth rates  $y_2$  of  $q = 2.0$  disks as functions of  $\log(M_*/M_d)$  for selected values of  $r_-/r_+$ . The  $m = 1$  modes are shown by blue solid lines,  $m = 2$  modes by red dotted lines,  $m = 3$  modes by blue dashed lines, and  $m = 4$  modes by black long-dashed lines.

where  $\mathcal{P}$  is the pressure tensor and  $\mathcal{I}$  is the unit tensor. The  $z$ -component of  $\mathbf{N}$  is responsible for radial angular momentum transport and is given by

$$N_z = \partial_t(\rho v_\phi \varpi) = -\nabla \cdot (\rho v_\phi \varpi \mathbf{v}) - \rho \partial_\phi \Phi_g. \quad (42)$$

The Reynolds stress is in the first term on the right hand side of Equation 42. The gravitational torque, composed of the disk self-interaction torque and the star-disk coupling torque, is the last term in the right hand side of the equation. The azimuthal pressure gradient term integrates to zero in our approximation.

Quasi-linear forms for the torque are found from substitution of

$$\rho = \rho_o + \delta\rho e^{im\phi}, \mathbf{v} = \mathbf{v}_o e^{im\phi}, \text{ and } \Phi_g = \Phi_{g,o} + \delta\Phi_g e^{im\phi} \quad (43)$$

into Equation 42. The gravitational self-interaction torque over the annulus between  $\varpi$  and  $\varpi + \Delta\varpi$  is

$$\Gamma_g = m\pi \int_{-Z_*}^{Z_*} dz \int_{\varpi}^{\varpi+\Delta\varpi} |\delta\rho| |\delta\Phi| \sin(\phi_\rho - \phi_\Phi) \varpi d\varpi \quad (44)$$

where  $\phi_\rho$  and  $\phi_\Phi$  are the phases of the density and gravitational perturbations (Imamura, Durisen, & Pickett 2000). The Reynolds stress arises from coupling of the azimuthal and radial velocity perturbations. The radial flux of angular momentum carried by waves is the Reynolds stress integrated over the cylindrical surface with radius  $\varpi$ ,

$$\mathcal{F}_R = \pi \int \rho_o |\delta v_\varpi| |\delta v_\phi| \cos(\phi_{v_\phi} - \phi_{v_\varpi}) \varpi^2 dz \quad (45)$$

(*e.g.*, see Shariff 2009). The Reynolds stress torque on the volume between  $\varpi$  and  $\varpi + \Delta\varpi$  is  $\Gamma_R = -\mathcal{F}_R(\varpi + \Delta\varpi) + \mathcal{F}_R(\varpi)$ . The  $\Gamma_g$  and  $\Gamma_R$  are calculated using eigenfunctions normalized such that

$$\mathcal{M}_m = \int |\delta\rho| d^3x = 1. \quad (46)$$

The torques scale as  $\mathcal{M}_m^2$  for arbitrary  $\delta\rho$  and are given in units of  $\Gamma_o = J/\tau_o$  where  $J$  is the total angular momentum. The characteristic angular momentum transport time,

$$\tau_\Gamma = \frac{J_z(\varpi)}{\Gamma_m} \quad (47)$$

where  $J_z(\varpi)$  is the  $z$ -component of the angular momentum in the annulus  $[\varpi, \varpi + \Delta\varpi]$ ,

$$J_z(\varpi) = \int_0^{2\pi} d\phi \int_{-Z_*(\varpi)}^{Z_*(\varpi)} dz \int_{\varpi}^{\varpi+\Delta\varpi} \hat{\mathbf{z}} \cdot (\mathbf{r} \times \rho \mathbf{v}) \varpi d\varpi,$$

$$(48)$$

$Z_*(\varpi)$  is the vertical height of the disk at given  $\varpi$ ,  $\Gamma_m = \Gamma_g + \Gamma_R$  and  $\tau_\Gamma$  is given in units of  $\tau_o$ . Properties of models selected for presentation are described in Tables 1 to 5 with their  $\Gamma_g$ ,  $\Gamma_R$ ,  $\delta J$ , and  $\tau_\Gamma$  shown in Figures 20 to 27. We designate the smallest radius where  $\tau_\Gamma = \tau_o$  as  $r_{1,-}$  and the next radius where  $\tau_\Gamma = \tau_o$  as  $r_{1,+}$ . In Table 5, the regions in the disks where  $\tau_\Gamma < \tau_o$ ,  $r < r_{1,-}$  and  $r > r_{1,+}$ , and the mass contained in those regions,  $m_{1,-}$  and  $m_{1,+}$ , the radius at which the first sign change in  $\Gamma_m$  falls,  $r_\Gamma$ , and the mass inside that radius,  $m_\Gamma$  are given.

### 3.4.1 $m = 4$ J Mode

J modes are dominated by the gravitational stress  $\Gamma_g$ . The  $\tau_\Gamma$ ,  $\delta J$ ,  $\Gamma_g$ , and  $\Gamma_R$  for a representative J mode, the dominant  $m = 4$  J mode for the  $M_*/M_d = 0.01$ ,  $q = 1.5$ ,  $r_-/r_+ = 0.402$  disk, Model J1, are shown in Figure 20. The eigenvalues for  $m = 4$  mode are  $(y_1, y_2) = (-0.378, 0.576)$ . Corotation sits at  $1.068 r_o$ . The inner Lindblad radius  $r_{ilr}$  falls near an extremum in  $\Gamma_m$  while  $r_{olr}$  is near  $r_+$ . The gravitational torque,  $\Gamma_g$  is negative inside  $\sim r_o$  and positive outside  $\sim r_o$ .  $\delta J$  and  $\Gamma_m$  also both change sign near  $r_o$ . Although the total torque  $\Gamma_m$  is dominated by  $\Gamma_g$ , the Reynolds stress torque  $\Gamma_R$  is not negligible in the inner half of the disk. The torque is strong in this disk and the disk expected to spread on time scales of  $\sim \tau_o$  as instability approaches  $\mathcal{M}_4 \sim 1$ . Material with inflow times  $< \tau_o$  fall at radius  $< 0.848 r_o$ , a region which contains 12 % of the disk mass and for  $r > 1.24 r_o$ , a region which contains 12 % of the disk mass. The sharp peak in  $\tau_\Gamma$  indicates where  $\Gamma_m$  goes to zero. Because this is a discrete calculation, the exact zero is stepped over in our simulation and the peak has finite amplitude. The narrow peak in the transport time indicates that only matter close to the zero in  $\Gamma_m$  will remain relatively stationary as the disk evolves. Up to 44 % of the disk mass has flow time less than  $2 \tau_o$  at saturation. The perturbed angular momentum  $\delta J$  and  $\Gamma_m$  follow each other's behavior suggesting that how and where instability is driven follows from  $\Gamma_m$ . Several other modes in this disk model are also unstable and, in fact, the dominant mode is not the  $m = 4$  J mode but, rather, it is an  $m = 1 I^+$  mode (see §3.4.5).

### 3.4.2 $m = 2$ I<sup>-</sup> Mode

The  $\tau_\Gamma$ ,  $\delta J$ ,  $\Gamma_g$ , and  $\Gamma_R$  for the  $m = 2 I^-$  modes for the  $q = 1.5$  disks with  $M_*/M_d = 0.1$  and  $r_-/r_+ = 0.402$  and  $M_*/M_d = 5$  and  $r_-/r_+ = 0.602$ , Models I1 and I2, respectively are shown in Figure 21. For Model I1, corotation sits inside  $r_-$  for this disk and  $r_{olr}$  sits near

Table 5: Mass Transport Properties

Model	Mode	$r_{(1,-)}/r_o, m_{(1,-)}$	$r_{(1,+)} / r_o, m_{(1,+)}$	$r_\Gamma / r_o, m_\Gamma$
J1	$m=4$ J	0.85,0.12	1.24,0.12	1.02,0.44
J1	$m=1$ I <sup>+</sup>	0.69,0.0053	1.11,0.36	0.77,0.040
I1	$m=2$ I <sup>-</sup>	0.84,0.023	1.14,0.090	1.07,0.71
I2	$m=2$ I <sup>-</sup>	0.80,0.0023	1.25,<0.001	0.96,0.28
I4	$m=2$ I <sup>+</sup>	0.83,0.10	1.29,0.071	1.07,0.73
I5	$m=2$ I <sup>+</sup>	0.71,0.050	1.32,<0.001	0.76,0.0060;1.08,0.33
O13	$m=1$ A	1.37,0.16	3.90,0.004	1.75,0.34
E1	$m=2$ Edge	0.73,0.0032	5.4,<0.0001	1.12,0.056
P2	$m=2$ P	0.79,0.0043	1.42,0.0050	1.09,0.51
O16	$m=1$ P	0.85,< 0.0001	1.21,< 0.0001	1.02,0.51

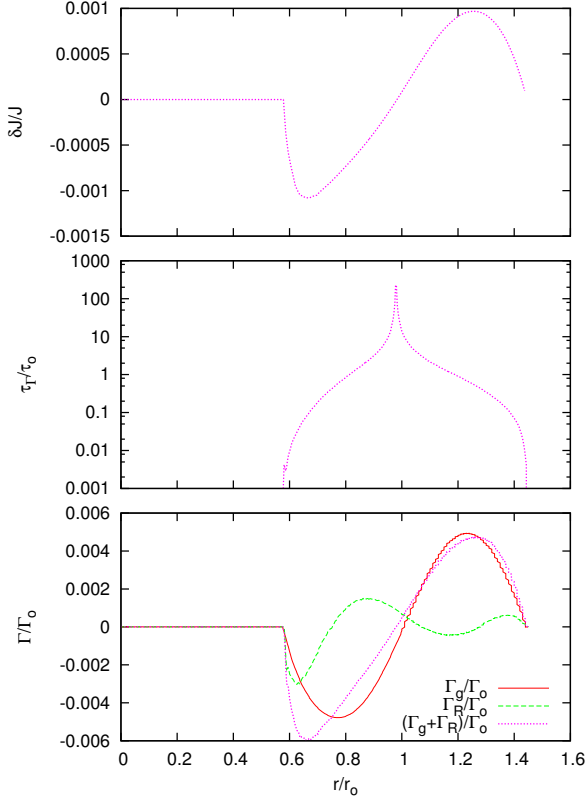


**Fig. 20** The  $\tau_r$ ,  $\delta J$ ,  $\Gamma_g$ , and  $\Gamma_R$  for the  $m = 4$  J mode of the  $M_*/M_d = 0.01$ ,  $q = 1.5$ ,  $r_-/r_+ = 0.402$  disk, model J1.

$r_o$  which is around where  $\Gamma_g$  peaks.  $\Gamma_g$  is negative in the inner part of the disk and positive in the outer part of the disk. The Reynolds stress dominates overall, but the gravitational stress cannot be ignored. The general shapes of  $\Gamma_m$  and  $\delta J$  are similar, strongly negative in the inner half of the disk and positive in the outer half of the disk. The zero of  $\Gamma_m$  lies at  $1.07 r_o$ , a region which contains 71 % of the disk mass. The disk transport times are generally long. Material with inflow time  $< \tau_o$  falls within radius  $r < 0.84 r_o$ , a region which contains 2.3 % of the disk mass and material with outflow time  $< \tau_o$  fall outside radius  $1.14 r_o$  a region which contains 9 % of the disk mass. The similar forms for  $\delta J$  and  $\Gamma_m$  support the suggestion that  $\Gamma_m$  indicates where and how instability is driven. For the I<sup>-</sup> mode of Model I2,  $\Gamma_g$  changes character.  $\Gamma_g$  is negative near the inner and outer edges of the disk and positive around  $r_o$ .  $\Gamma_R$  tracks  $\delta J$  more closely than does  $\Gamma_g$ . Instability is driven primarily by  $\Gamma_R$  although  $\Gamma_g$  is not negligible. For this mode only 28 % of the disk mass falls within the sign change in  $\Gamma_m$  with only 0.23 % of the disk mass having inflow time  $< \tau_o$ . This disk model is expected to evolve only slowly.

### 3.4.3 $m = 2$ I<sup>+</sup> Mode

The  $\delta J$ ,  $\tau_r$ ,  $\Gamma_g$ , and  $\Gamma_R$  for the  $m = 2$  I<sup>+</sup> mode from  $q = 1.5$  disks, and  $M_*/M_d = 7$  and  $r_-/r_+ = 0.5$ , and  $M_*/M_d = 0.2$  and  $r_-/r_+ = 0.602$ , Models I5 and I4, respectively are shown in Figure 22. For Model I5 corotation sits outside  $r_o$  just inside  $r_+$ . The  $\delta J$  differs qualitatively from that in the I<sup>-</sup> mode.  $\delta J$  is positive in the inner and outer thirds of the disk and negative in the central region of the disk. The Reynolds stress and gravitational stress are both important for this mode, however,  $\Gamma_g$  tracks  $\delta J$  more closely than does  $\Gamma_R$ .  $\Gamma_g$  is positive in the inner and outer thirds of the disk and negative in the middle portion of the disk. Near the inner edge of the disk,  $r < 0.71 r_o$ , the transport will be

outward on times less than  $\tau_o$ . It is possible that the inner 0.05 % of the disk mass inhibits accretion onto the star. Between  $0.76$  and  $1.08 r_o$ , a region which contains two-thirds of the disk mass,  $\Gamma_m < 0$  and the material is expected to flow inward. Outside  $1.08 r_o$ ,  $\Gamma_m$  changes sign again and we expect the outer third of the disk mass to flow outward. The results for the  $I^+$  mode for the small  $M_*/M_d$  disk, model I4 are more similar to those for the  $I^-$  mode. The  $I^+$  mode results discussed here and the  $I^-$  mode results discussed in §3.4.2 suggest that the properties of I modes are more strongly affected by  $M_*/M_d$  than by whether they are an  $I^-$  or an  $I^+$  mode.

#### 3.4.4 $m = 2$ P & Edge Modes

The evolution of P modes and edge modes is expected to be qualitatively different from that of J modes and to show differences in detail from I modes. We show  $\Gamma_g$ ,  $\Gamma_R$ ,  $\tau_\Gamma$ , and  $\delta J$  for representative  $m = 2$  modes of an  $M_*/M_d = 10^2$ ,  $q = 2$ , system with  $r_-/r_+ = 0.5$  and  $0.101$ , Models P2 and E1, in Figures 23 and 24. The small  $r_-/r_+$  disk shows an edge mode and the larger  $r_-/r_+$  disk shows a P mode. First consider the P mode. The Reynolds stress dominates the disk, the gravitational stress is negligible for this mode.  $\Gamma_m$  is strongly negative in the inner region of the disk, decreasing angular momentum and driving the inner disk inward. Material inside  $r = 0.80 r_o$  (the inner 0.5 % of the disk mass) has inflow time  $< \tau_o$ . The region where  $\Gamma_m < 0$  ends at  $r = 1.09 r_o$  (and contains 51 % of the disk mass). The stress is weak most of the disk has  $\tau_\Gamma > \tau_o$ . Comparison of  $\delta J$  and  $\Gamma_m$  suggests that, although  $\delta J$  changes sign slightly outside where  $\Gamma_m$  changes sign their shapes are nearly the same, suggesting that  $\Gamma_m$  once again indicates where and how instability is driven.

Edge modes are dominated by the Reynolds stress with the total stress  $\Gamma_m$  strongly negative near the inner edge of the disk as can be seen in Figure 24 where we show  $\tau_\Gamma$ ,  $\delta J$ ,  $\Gamma_g$ , and  $\Gamma_R$  for an  $m = 2$  edge mode for an  $M_*/M_d = 10^2$ ,  $q = 2$ ,  $r_-/r_+ = 0.101$  disk, Model E1. The bottom panel shows the  $\Gamma$  plotted on the same axes. The next panel up shows  $\Gamma_g$  on rescaled axes to show its form compared to  $\Gamma_R$ . The transport time is smallest near the inner edge of the disk where for material inside  $r = 0.73 r_o$  (0.32 % of the disk mass) the inflow time  $< \tau_o$ . The region inside the first zero of  $\Gamma_m$  contains only 5.6 % of the disk mass, it does contain the density maximum, however. Based on quasi-linear modeling, we expect rapid accretion of 0.3 % of the disk mass to occur; the bulk of the disk mass will not take part. The angular momentum perturbation  $\delta J$  and  $\Gamma_m$

vary together for the most part. There are differences, however, and the case for direct correlation is less compelling. As also true for P modes, instability for this multi-armed mode is driven by the Reynolds stress.

#### 3.4.5 $m = 1$ $I^+$ , A, and P Modes

The  $\tau_\Gamma$ ,  $\delta J$ ,  $\Gamma_g$ , and  $\Gamma_R$  for the dominant  $m = 1$   $I^+$  mode from the  $M_*/M_d = 0.01$ ,  $q = 1.5$ , and  $r_-/r_+ = 0.402$  disk, Model J1, are shown in Figure 25. The mode is slow with  $(y_1, y_2) = (-0.986, 1.210)$  so that  $r_{co} > r_+$ .  $\Gamma_g$  and  $\Gamma_R$  both play roles in the torque, however,  $\Gamma_R$  dominates outside  $r_o$  while  $\Gamma_g$  and  $\Gamma_R$  are comparable in magnitude in the inner half of the disk. Similarly to the  $I^-$  and  $I^+$  multi-armed modes,  $\Gamma_R$  is positive in the inner region of the disk. The large  $\Gamma_g$  in the inner half of the disk arises even though this is an  $I^+$  mode because of the star/disk couple. We find that  $\Gamma_m$  is negative over most of the disk because of the star/disk couple. The inner region of the disk,  $r < 0.69 r_o$  with mass  $5 \times 10^{-3}$ , feels positive torque and not expected to accrete onto the star. For  $r > 0.76 r_o$  which contains 96 % of the mass of the disk, the torque is negative and material is expected to flow inward. The angular momentum lost by the disk drives orbital motion of the star about the center-of-mass of the system. However, the outer 36 % of the disk mass will flow inward on time scales  $< \tau_o$  tending to narrow the disk. The perturbed angular momentum  $\delta J$  is positive in the inner region of the disk similarly to the earlier  $I^+$  mode discussed in contrast to the other cases shown where  $\delta J < 0$  near the inner edge of the disk. Comparison of  $\delta J$  and  $\Gamma_m$  suggests that, although  $\delta J$  changes sign slightly outside where  $\Gamma_m$  changes sign, their similarity indicates that  $\Gamma_m$  shows where and how instability is driven.

A modes arise in  $q \sim \sqrt{3}$  systems with  $M_*/M_d \sim 0.5$  to 5, and small  $r_-/r_+$ . We did not find A modes in  $q = 1.5$  and 2 systems.  $\Gamma_g$ ,  $\Gamma_R$ ,  $\tau_\Gamma$ , and  $\delta J$  for the  $M_*/M_d = 1$ ,  $q = 1.8$  disk with  $r_-/r_+ = 0.101$  disk, Model O13, are shown in Figure 26 For this mode, corotation sits outside  $r_o$  similar to  $I^+$  modes and similar to  $I^+$  modes,  $\Gamma_R$  is positive in the inner region of the disk and  $\Gamma_g$  and  $\Gamma_R$  are competitive in this disk with  $\Gamma_g$  dominating near the inner edge of the disk while  $\Gamma_R$  plays a more important role in the middle to outer regions of the disk. The overall torque is generally negative and the disk loses angular momentum to the central star. As noted earlier, the mode is slow with  $r_{co}/r_o = 1.53$  and Lindblad outer resonance at  $r_{olr}/r_{co} = 2.01$ . The transport time for the A mode is short; inside  $r = 1.37 r_o$  the inflow time is  $< \tau_o$  a region which contains 16 % of the disk mass. The region which has  $\Gamma_m < 0$  is within  $r < 1.75 r_o$  with contains 34 % of the disk mass.

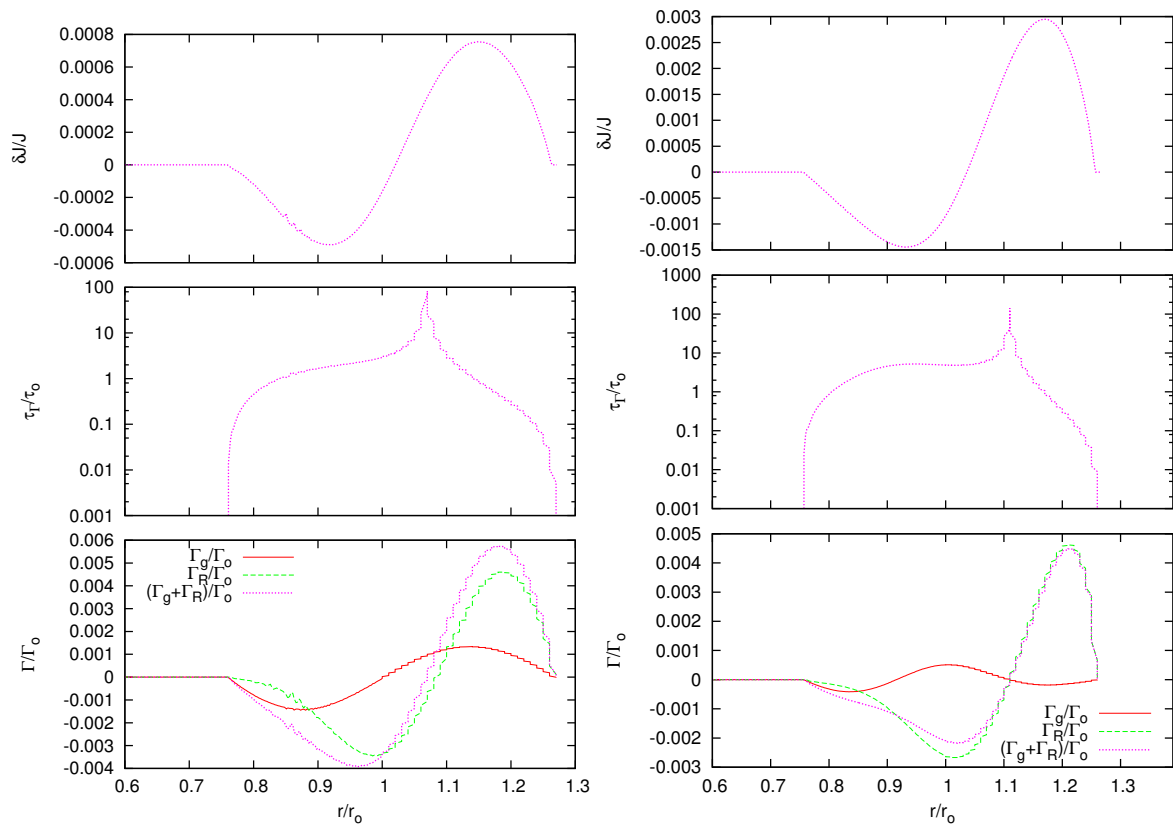


**Fig. 21** The  $\tau_r$ ,  $\delta J$ ,  $\Gamma_g$ , and  $\Gamma_R$  for the  $m = 2 \Gamma^-$  mode for  $q = 1.5$ ,  $r_-/r_+ = 0.602$  disks with  $M_*/M_d = 0.1$  and 5, Models I1 (left column) and I2 (right column), respectively.

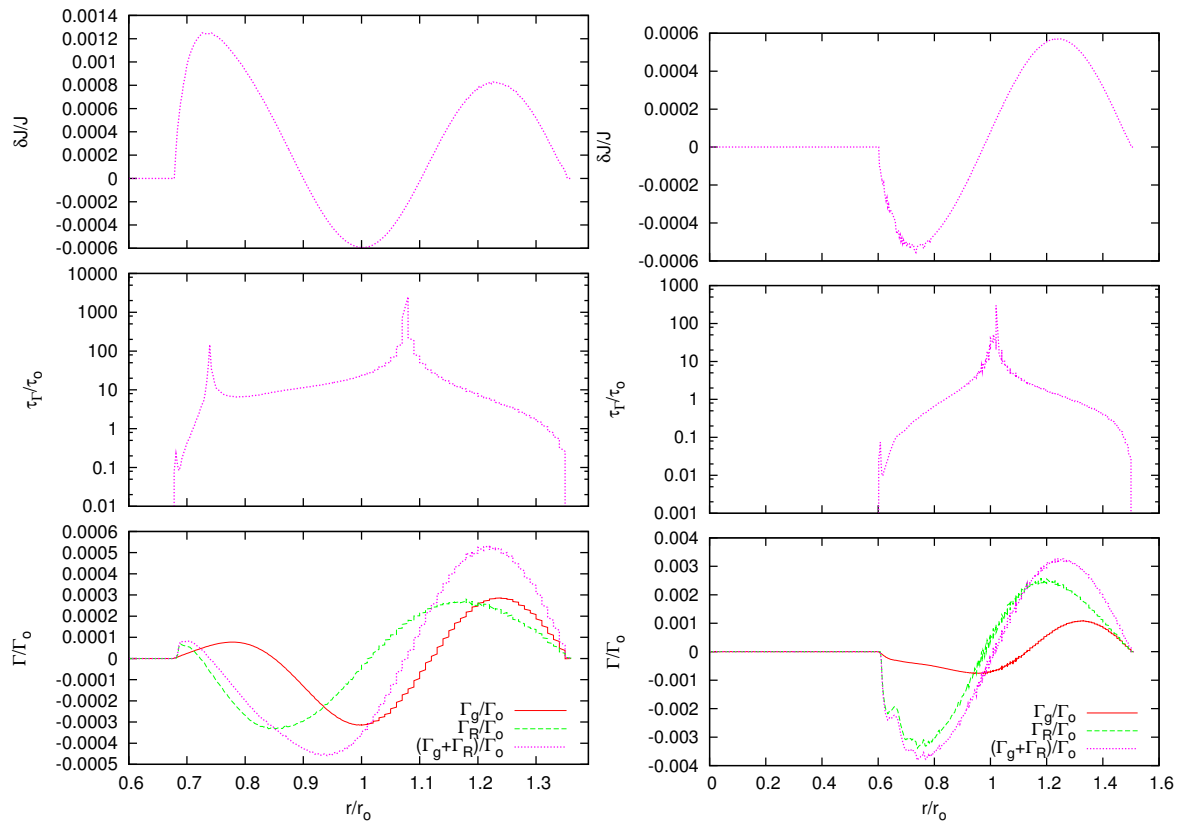


**Fig. 22** The  $\tau_\Gamma$ ,  $\delta J$ ,  $\Gamma_g$ , and  $\Gamma_R$  for the  $m = 2 I^+$  modes for  $q = 1.5$  disks with  $M_*/M_d = 7$ , and  $r_-/r_+ = 0.5$ , Model I5 (left column).  $M_*/M_d = 0.2$  and  $r_-/r_+ = 0.402$ , Model I4 (right column).

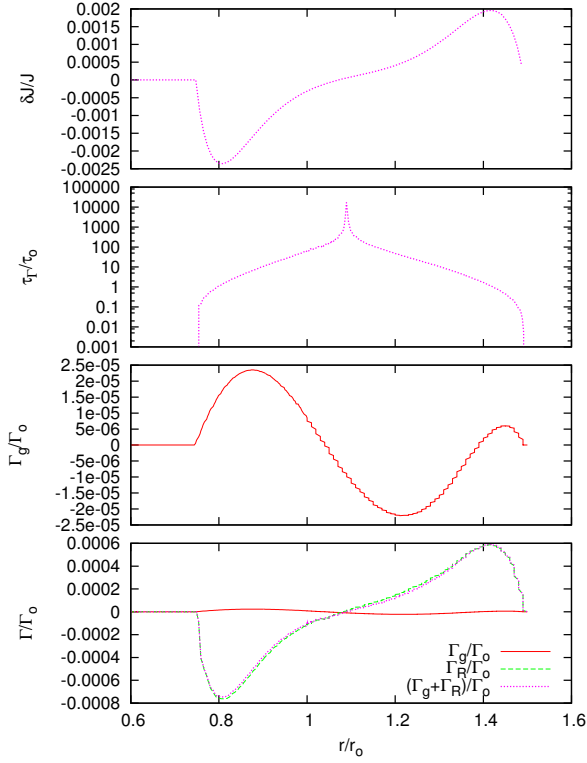


**Fig. 23** The  $\tau_T$ ,  $\delta J$ ,  $\Gamma_g$ , and  $\Gamma_R$  for the  $m = 2$  P mode in the  $M_*/M_d = 100$ ,  $q = 2$ ,  $r_-/r_+ = 0.5$  disk, model P2.

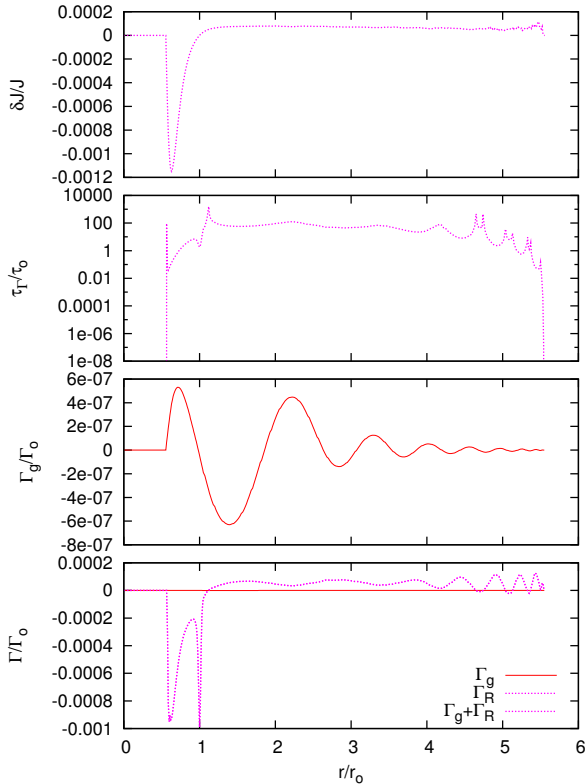


**Fig. 24** The  $\tau_T$ ,  $\delta J$ ,  $\Gamma_g$ , and  $\Gamma_R$  for the  $m = 2$  edge mode in the  $M_*/M_d = 100$ ,  $q = 2$ ,  $r_-/r_+ = 0.101$  disk, model E1.

The angular momentum transport time,  $\tau_T < 2\text{--}3 \tau_0$  over much of the disk and disk spreading is expected as the nonlinear regime is approached. Comparison of  $\delta J$  and  $\Gamma_m$  suggests that, although  $\delta J$  changes sign slightly outside where  $\Gamma_m$  changes sign, their general similarity indicates that  $\Gamma_m$  shows where and how instability is driven.

We show  $\Gamma_g$ ,  $\Gamma_R$ ,  $\tau_T$ , and  $\delta J$  for a disk with large  $M_*/M_d$ , Model O16, in Figure 27. The mode has  $(y_1, y_2) = (-0.0222, 0.134)$  and corotation sits near  $r_0$ . We classify the mode as a P mode. It is different from other P modes because even though the disk is dominated by  $\Gamma_R$ ,  $\Gamma_g$  is not negligible. Self-gravity is not negligible likely because the disk is narrow,  $r_-/r_+ = 0.70$ ; the inner edge of the disk sits far from the star and so is less affected by the star’s tidal field.  $\Gamma_m$  is strongly negative inside  $r_0$  and positive outside  $r_0$  suggesting that the disk will have a tendency to spread as instability grows. However,  $\Gamma_m$  is weak and  $< 0.01\%$  of the mass is expected to flow inward and outward on timescales of  $\tau_0$  as  $\mathcal{M}_1$  approaches 1. The disk does not tend to redistribute angular momentum efficiently as nonlinearity is approached. Comparison of  $\delta J$  and  $\Gamma_m$  suggests  $\Gamma_m$  again offers support for the suggestion that  $\Gamma_m$  indicates where and how instability is driven.

## 4 DISCUSSION

### 4.1 Comparison to Previous Work

The work most directly comparable to ours is that of Woodward, Tohline, & Hachisu (1994, WTH). WTH performed nonlinear simulations of  $(n, q) = (1.5, 2)$  disks; 15 simulations with full  $2\pi$  coverage in azimuth to study  $m = 1$  modes and 19 simulations with  $\pi$ -symmetry to study even  $m$  modes. WTH modeled star/disk systems with  $M_*/M_d = 0.2, 1, \text{ and } 5$  and repeated seven toroid ( $M_*/M_d = 0.0$ ) simulations reported by Tohline & Hachisu (1990) (see also Hadley & Imamura 2011). WTH usually used numerical grids of size  $64 \times 32 \times 64$ , radial  $\times$  vertical  $\times$  azimuthal zones. For some narrow disks, WTH used  $128 \times 32 \times 64$  resolution. For our simulations, we typically used grids of dimension, radial  $\times$  vertical zones, given by  $512 \times 512$ . For some models we used grids as large as  $1,024 \times 1,024$ . Because of the difference in zoning, we opted for  $r_-/r_+$  values which produced disks that matched the  $T/|W|$  values given in WTH rather than matching  $r_-/r_+$  values. Figure 28 shows comparisons for the  $y_1$  and  $y_2$  values. Overall, the agreement is good. Differences, when they arise, are quantitative in nature.



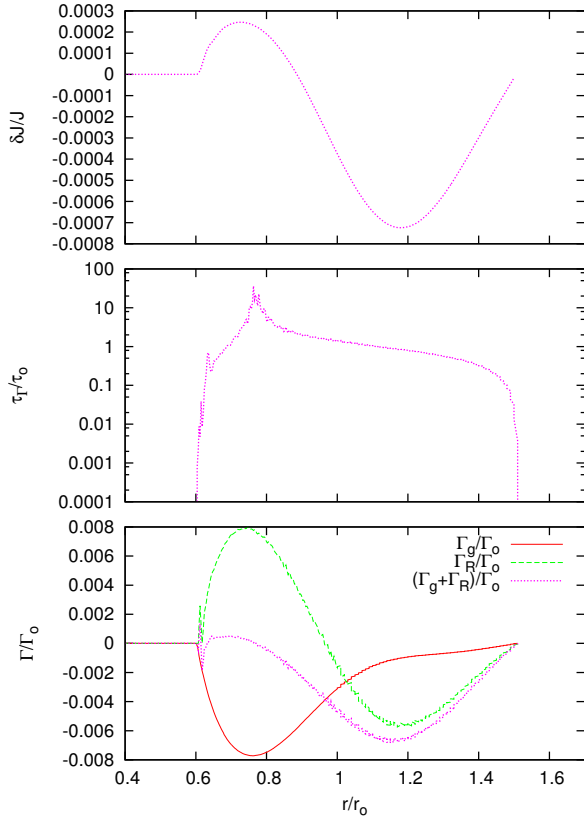


**Fig. 25** The  $\tau_\Gamma$ ,  $\delta J$ ,  $\Gamma_g$ , and  $\Gamma_R$  for the  $m = 1$  I<sup>+</sup> mode in the  $M_*/M_d = 0.01$ ,  $q = 1.5$ ,  $r_-/r_+ = 0.402$  disk, model J1.

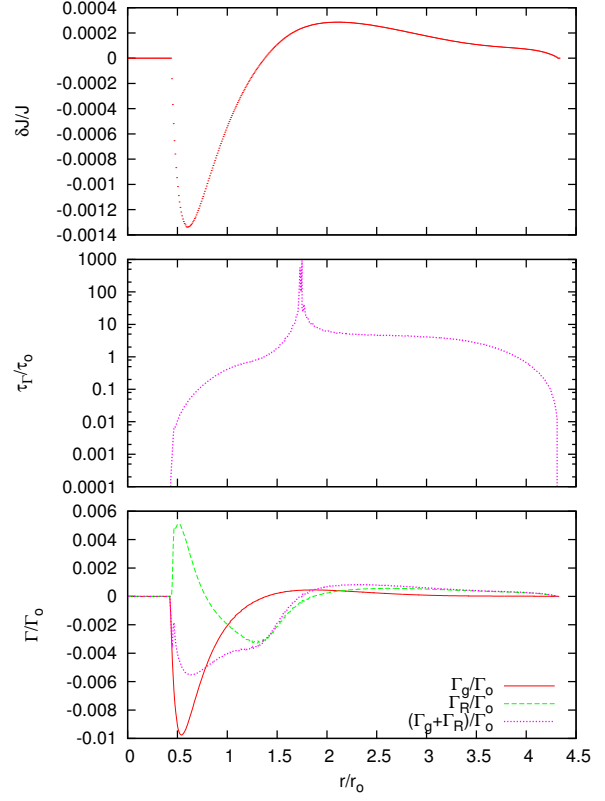


**Fig. 26** Q5  $\tau_\Gamma$ ,  $\delta J$ ,  $\Gamma_g$ , and  $\Gamma_R$  for the  $m = 1$  A mode in the  $M_*/M_d = 1.0$ ,  $q = 1.8$ ,  $r_-/r_+ = 0.101$  disk, model O13.

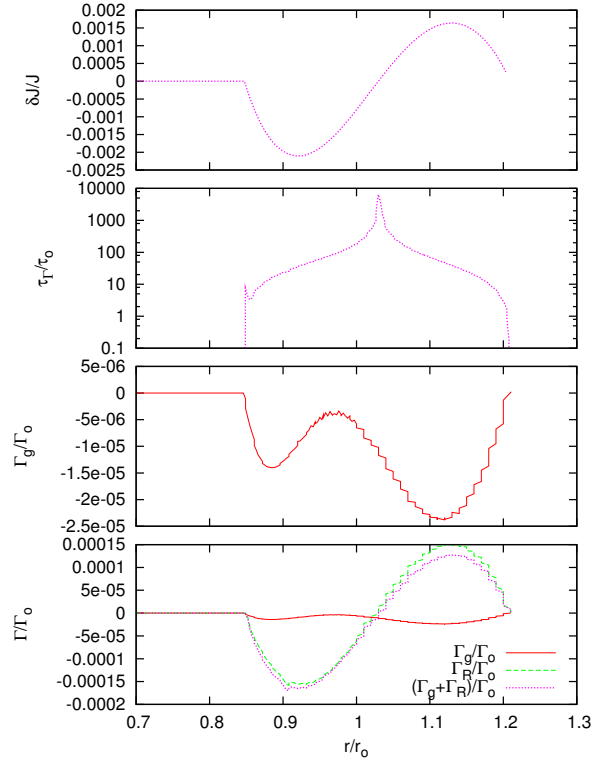


**Fig. 27** Q8  $\tau_\Gamma$ ,  $\delta J$ ,  $\Gamma_g$ , and  $\Gamma_R$  for an  $m = 1$  P mode in a  $M_*/M_d = 100$ ,  $q = 2$ ,  $r_-/r_+ = 0.7$  disk, model O16.

We begin our comparison with the  $m = 1$  results. For the lowest star mass case,  $M_*/M_d = 0.2$ , the eigenvalues agree to within 10 % and the eigenfunction phase plots are similar exhibiting edge-like mode character through  $T/|W| \sim 0.22$  after which the phase plots take on characteristics associated with I and P modes. However, the existence of P modes for  $M_*/M_d = 0.2$  disks would be surprising because even weak self-gravity has been shown to suppress P modes (Goodman & Narayan 1988). The *low* oscillation frequency measured for the modes,  $y_1 \sim -0.7$ , places corotation radius well outside  $r_o$ , in contrast to massive star systems and non-self-gravitating disks where we find that corotation sits near  $r_o$ . For NSG disks where P modes are unambiguously identified, even for the system with a very wide disk,  $r_-/r_+ \sim 0.4$ , the oscillation frequency  $y_1 = -0.16$ . NSG narrow disks where  $r_-/r_+ > 0.6$ , show  $y_1 < -0.1$ . That is, even for cases where corotation does not sit precisely at  $r_o$ , corotation is still close to  $r_o$  for small  $T/|W|$  and approaches  $r_o$  as  $T/|W|$  increases in NSG systems. These results suggest that the modes in SG systems are  $I^+$  modes, not P modes. Our results and those of WTH are in good agreement. For the higher star mass sequence,  $M_*/M_d = 1$  sequence, we find similarly good agreement. We again see edge-like mode behavior at low  $T/|W|$ , persisting to  $T/|W| = 0.253$ . Beyond  $T/|W| = 0.253$ , the disturbance again takes on the appearance of an I and/or P mode. By  $r_-/r_+ \sim 0.6$ , where  $T/|W| \sim 0.42$ , the phase diagram strongly resembles that for modes in NSG disks. The  $y_1$  are, however, still small,  $-0.36$ . Although the modes have appearances of P and/or I modes, because corotation falls well outside  $r_o$  we identify the modes as  $I^+$  modes. Our results for  $M_*/M_d = 1$  match closely those of WTH. The results for the  $M_*/M_d = 5$  sequence are not in as good quantitative agreement. However, direct comparison of our work to that of WTH for  $M_*/M_d = 5$  models is difficult because the nonlinear simulations of WTH were only in the *linear* regime for, at most, a couple of rotation periods.

Consider next the results for  $m \geq 2$  modes. Start with the  $M_*/M_d = 0.2$  sequence. Our results and those from WTH agree well. Both indicate a stable model at  $T/|W| = 0.22$ , an unstable leading phase shift I mode at  $T/|W| = 0.26$ , changing to a trailing arm I mode at  $T/|W| = 0.29$ . The plot of the comparison of  $y_1$  and  $y_2$  values for  $m = 2$ ,  $M_*/M_d = 1$  sequences are similar with our  $y_2$  values approximately 10 % larger in magnitude than those in WTH. Also, our  $y_1$  values are close to those in WTH and indicate that corotation is near the inner edge of the disk. The WTH phase plot for the  $T/|W| = 0.422$  is not well resolved and is difficult to use for comparison (Woodward 1994). Our linear

model took  $10 \tau_o$  to settle into a mode and the nonlinear calculation had organized and saturated before that much time had elapsed. There were discrepancies in the last sequence of models, the  $M_*/M_d = 5$  sequence. To clarify the situation, we added results for disk systems over a wider range in  $T/|W|$  than considered by WTH to the comparison plot. We see that the discrepancies arise in the region where a mode change occurs. In fact, the eigenvalues for the  $T/|W| = 0.42$  and  $0.43$  models have been indicated to be uncertain by WTH, with the modes identified as L modes.<sup>2</sup> The phase plots of these models (Woodward 1994) are hard to compare with ours, but we agree that corotation lies nearly at  $r_o$ . Our eigenfunction plots in this region indicate a small second dip just beginning to emerge. Such a feature would not be visible in the phase plots of WTH which are too noisy (see Woodward 1994). The next two higher  $T/|W|$  models considered by WTH were also classed by them as L modes with no uncertainty indicated in their growth rates. However, growth in these models saturated at low amplitude. Our calculations for these two models disagree. We find that  $m = 2$  modes in these models are stable showing no hint of growth after  $40 \tau_o$ . The last three models qualitatively agree between the studies as far as the I mode nature of the plots and the values of the growth rates. There is agreement in the  $y_1$  values for the  $T/|W| = 0.46$  model while the other  $y_1$  values were not reported by WTH. We investigate this regime in a later paper where in a larger study we apply our linear and quasi-linear theories and nonlinear modeling to study the early nonlinear behavior in a wide range of disk models unstable to I, J, P, edge, and  $m = 1$  modes in order to determine how they manifest themselves in the nonlinear regime in terms of their angular momentum transport properties (Hadley *et al.* 2013).

## 4.2 Be Stars

Be stars are emission line systems composed of rapidly rotating Main Sequence B type stars with circumstellar disks (*e.g.*, see Okazaki 1997). In general, they exhibit double-peaked hydrogen emission lines indicating the existence of circumstellar disks. Further, several Be star systems show long-period quasi-periodicity in the relative intensity of the violet (V) and red (R) components of their double-peaked emission lines. The V/R quasi-variability occurs on periods ranging from years

<sup>2</sup> WTH suggested that some star/disk systems exhibited *super-critical stability* (Landau & Lifshitz 1987, Drazin & Reid 2004) in that some linearly unstable modes would saturate at low amplitudes and not disrupt the systems. WTH referred to these modes as L modes.

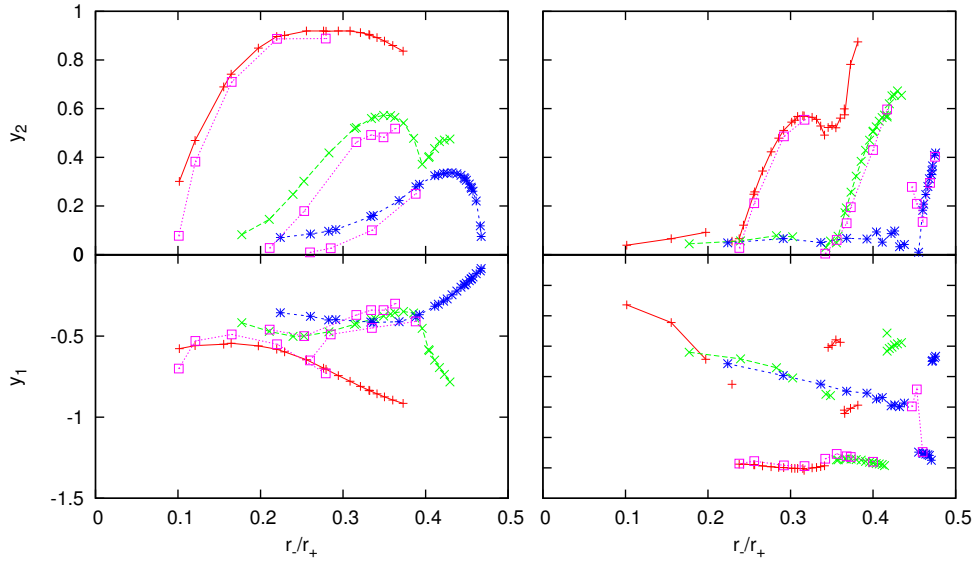


**Fig. 28** The  $m = 1$  and 2 eigenvalue comparison for disk sequences with  $n = 1.5$ ,  $q = 2$  and  $M_*/M_d = 0.2, 1$ , and 5. Our eigenvalues are the green line symbols and those from WTH are marked by the red dashed-line symbols.

to decades with a statistical mean on the order of 7 y, a period much longer than the rotation periods of the stars and much longer than the orbital periods of material in typical circumstellar disks unless the disks extend to great distances from the Be star. A model proposed for the V/R variability was the excitation of  $m = 1$  modes in nearly Keplerian disks (*e.g.*, Kato 1983). Typically, the excitation mechanism for such  $m = 1$  modes has not been identified except for binary star systems where tidal forcing due to the companion could drive  $m = 1$  modes and for massive disk systems where coupling between the disk and central star could drive oscillations (*e.g.*, Adams, Ruden, & Shu 1989). Optical interferometric observations have indicated the existence of prograde  $m = 1$  modes in the binary Be star system  $\zeta$  Tau (Vakili *et al.* 1998), and the early-type Be star system  $\gamma$  Cas (Berio *et al.* 1999) while the disks are in Keplerian motion (*e.g.*, see Vakili, Mourard, & Stee 1994).

Early theoretical work on the  $m = 1$  modes of nearly Keplerian disks showed that pressure forces naturally led to low-frequency retrograde modes (Kato 1983, Okazaki 1991). Later works showed that a gravitational quadrupole moment (as expected for the rapidly rotating stars in Be systems) overcame pressure effects and led to disks with prograde  $m = 1$  oscillations. Okazaki (1997) argued that such a solution was viable only for late-type Be star systems where disks were likely to be cold. The early-type  $\gamma$  Cas system required another explanation which Okazaki (1997) suggested was radiative line forcing. Pappalozou & Savonije (2006)

then showed that for a free inner boundary, the  $m = 1$  modes were prograde. The aforementioned works all considered thin, two-dimensional disks. Ogilvie (2008) showed that in fat disks (three-dimensional disks), prograde  $m = 1$  modes were possible for point mass stars independent of the inner boundary condition. In our work, self-excited, long-period,  $m = 1$  modes appear in self-gravitating, thick Kepler-like disks. Kepler-like disks for  $M_*/M_d > 5$ , and  $r_-/r_+ = 0.05$  to 0.2 show low-frequency,  $|\omega_1| \ll \Omega_o$   $m = 1$  modes which can be either prograde or retrograde depending upon the system. At the lower end of the parameter range,  $m = 1$  modes are retrograde. For the higher  $M_*/M_d$  end of the range,  $m = 1$  modes switch to prograde for small  $r_-/r_+$ , that is, when self-gravity and pressure forces in the disk are weaker,  $m = 1$  modes may be prograde whereas when the disk self-gravity and pressure forces are stronger,  $m = 1$  modes are retrograde. This suggests that for large  $M_*/M_d$  and small  $r_-/r_+$ , self-gravity dominates pressure forces causing the  $m = 1$  mode to be prograde. For lower  $M_*/M_d$ , pressure forces dominate self-gravity leading to retrograde  $m = 1$  modes.

### 4.3 Excitation of Disk Modes

The excitation and growth of  $m = 1$  modes in star/disk systems could couple the star and disk and drive otherwise stable nonaxisymmetric modes in the disk unstable. To see this, recall how we incorporated the effects of the indirect potential in our calculations (§3.1). We considered the indirect potential as an expansion of the

point mass potential where the position of the star was treated as a perturbation in that the magnitude of the perturbed stellar position,  $|\delta_*|$ , was assumed to be much smaller than the radius of the inner edge of the disk,  $r_-$ . In our first-order calculation, the orbiting star interacted with the unperturbed disk and the perturbed disk interacted with the unperturbed star. In this way, we self-consistently followed linear growth of  $m = 1$  disk modes. For disk modes with  $m \geq 2$ , no coupling occurs. However, once the  $m = 1$  mode reaches nonlinear amplitude, the indirect potential may then couple strongly to stable disk modes and drive  $m \geq 2$  instabilities in the disk. This could have implications for the nature of the angular momentum transport that arises from  $m = 1$  modes. If high- $m$  modes are driven, then the induced transport in the disk may act as a local transport rather than a global mechanism as would be expected from our simulations. A similar problem has been studied in the context of migration of planetary cores in protoplanetary disks (*e.g.*, see Papaloizou & Terquem 2006).

Another mode of interaction between the star and disk could come from coupling of internal stellar modes and disk modes. Such interactions have not been studied except in a handful of investigations, and, even then, the studies were in the context of star/disk coupling which drove secular instability in the central star and not instability in the surrounding disk. For example, Imamura *et al.* (1995) considered the coupling of  $m \geq 2$   $f$ -modes in secularly unstable polytropic stars with a surrounding disk to drive instability in the central star (see also Yuan & Cassen 1985) and Lai (2001) considered coupling of  $m \geq 2$   $f$ -modes in secularly unstable neutron stars and surrounding accretion disks to drive instability in the neutron star. Imamura *et al.* (1995) were interested in how rapidly rotating protostars could shed angular momentum and how the inner regions of protostellar disks were truncated while Lai (2001) was interested in whether  $f$ -mode instabilities could be driven in rapidly rotating neutron stars and so limit the spin rate of *millisecond* pulsars. In both Imamura *et al.* and Lai, internal stellar modes were calculated but the disk modes were not. It was assumed the time-varying nonaxisymmetric gravitational potential arising from the internal stellar modes drove spiral waves in the disks. The coupling torque was based on the approximation that the disk was thin and the coupling arose from the excitation of spiral waves at the the Lindblad and corotation resonances in the disk (see Papaloizou & Terquem 2006).

More recently Lin, Krumholz and Kratter (2011) modeled the collapse of an isothermal sphere of gas into a star-disk system, and investigated the effect of  $m = 1$

and  $m = 2$  disk modes on the evolution of the stars spin rate. In contrast to Lai and Imamura *et al.*, it was the disk modes that were calculated while the stellar modes were not. Lin, Krumholz and Kratter found that the  $m = 1$  dominant disk drove orbital motion of the star's center of mass, inhibiting spin evolution, while the  $m = 2$  dominant disk provided long-term gravitational spin-down torques.

#### 4.4 AB Aurigae and Protostellar Disks

AB Aurigae (AB Aur) is a well-observed Herbig-Haro Ae star, mass  $M_* = 2.4 \pm 0.2 M_\odot$  and age  $4.0 \pm 0.1$  My (de Warf *et al.* 2003), surrounded by a large, circumstellar disk, mass estimated as  $M_d = 0.02$  to  $0.1 M_\odot$  (Henning *et al.* 1998). *Subaru* (Takami *et al.* 2002) observations show that the disk in AB Aur has structure from its inner regions  $< 22$  astronomical units (A.U.) (Hashimoto *et al.* 2011) to its outer regions 554 A.U. (Fukugawa *et al.* 2004, Hashimoto *et al.* 2011) so that the disk in AB Aur is wide  $r_-/r_+ < 0.04$ . The characteristic time scale for the disk in AB Aur is  $\tau_o \sim 2\pi r/v_{orb}(r) \sim 10^3 (r/10^2 A.U.)^{1.5} (M_*/M_\odot)^{-0.5}$  y under the assumption the disk is in Keplerian motion. For the inner disk region,  $\tau_o \sim 600$  y and for the outer disk region  $\tau_o \sim 2,000$  y. Although these characteristic times are only a small fraction of the star formation time scale and AB Aur's estimated age, the times are not negligible and features associated with them could plausibly be observed. Consequently, features attributed to physical processes that operate on disk dynamical time scales, processes such as gravitational instability, could play roles in the formation of the structure observed in AB Aur. We consider this possibility here.

High-resolution observations of AB Aur have revealed two elliptical rings with major axes  $\sim 92$  A.U. and 210 A.U., separated by an elliptical gap with major axis 170 A.U. in AB Aur's disk (Fukugawa *et al.* 2004, Hashimoto *et al.* 2011). The rings have small eccentricity on the sky but are thought to be circular in shape; the eccentricity arising from inclination of the AB Aur system to the plane of the sky (Hashimoto *et al.* 2011). The ring/gap structure is seen in optically thick IR emission (Fukugawa *et al.* 2004) and optically thin sub-millimeter emission (Henning *et al.* 1998) suggesting that the features extend to the midplane of the disk and are more than corrugations in the surface density. The polarimetric high-resolution images obtained by the *Subaru* telescope have also revealed the presence of several dips in the intensity of the rings interpreted as spiral structures (Hashimoto *et al.* 2011). Hashimoto *et al.* (2011) found seven narrow dips with the most prominent, Dip A at  $\sim 10^2$  A.U.. Hashimoto

*et al.* (2011) did not detect point-like structures in Dip A, as would be expected if the gap was cleared by a massive protoplanet (however, see Oppenheimer *et al.* 2008). Hashimoto *et al.* noted that the appearance of the multi-armed spiral structure of AB Aur’s disk was consistent with expectations of gravitational instability (GI). However, they argued that GIs were not likely to be the explanation for the structure because of the large Toomre  $Q$ -parameter estimated for the disk,  $Q \sim 10$  (Pietu, Guilloteau, & Dutrey 2005). Other explanations such as gaps cleared by massive planetary cores (*e.g.*, Papaloizou & Terquem 2006) and spiral patterns excited by low-mass planetary cores (*e.g.*, Tanaka, Takeuchi, & Ward 2002) were proposed, but such scenarios may suffer from the lack of detected point-like sources (especially in in Dip A).

Our simulations find disk systems with  $M_*/M_d > 24$  and small disk aspect ratios,  $r_-/r_+ < 0.1$ , are unstable to low- $m$  tightly wound spiral modes in disks with  $q \sim 2$ . Low  $m$  edge modes would appear to show multiple dips when tightly wound. For an adiabatic disk with  $q = 2$ ,  $r_-/r_+ = 0.1$ , and  $M_*/M_d = 25$ , the Toomre  $Q$  parameter  $Q > 10$  everywhere in the disk. However, the disk is unstable to tightly wound nonaxisymmetric instabilities (E modes). See Figure 4 for the  $m = 2$  mode. The mode has eigenvalues  $(y_1, y_2) = (0.48, 0.056)$  with disk torques,  $\Gamma_g$  and  $\Gamma_R$ , shown in Figure 24. It shows a small inner bar, forward  $\pi/2$  phase jump, followed by trailing arms with very large winding number. At an  $M_*/M_d = 25$  self gravity is a relatively small factor, with the self-gravity parameter,  $p = 0.110$ .

AB Aur may be a transitional disk with the dust distribution a vestige of the original gas disk structure.

## 5 SUMMARY

We studied the I, J, P, and edge modes of hot, isentropic disks including self-gravity. We considered disk material with polytropic index  $n = 1.5$ , and disks with power law angular velocity distributions, exponents  $q = 1.5, 1.75$ , and 2, star-to-disk mass ratios,  $M_*/M_d = 0$  to  $10^3$  (from purely self-gravitating to almost non-self-gravitating), and inner-to-outer disk radii,  $r_-/r_+ = 0.05$  to 0.75. The parameter space covers that occupied by protoplanetary and protostellar disks.

We provide a brief summary of mode types, and then discuss our findings. Broadly, our equilibrium models had  $p \gtrsim 7.5$  for models identified as J modes,  $3 \lesssim p \lesssim 7.5$  for models identified as I modes and  $p \lesssim 3$  for models identified with P and edge modes (the P/I threshold being slightly higher for higher  $m$ ). The  $I^-/I^+$  boundary, depending on  $q, m$ , is typically from  $r_-/r_+$  of .5 to .7, increasing with both parameters as well as  $M_*/M_d$ .

J modes are strongly self-gravity driven, I modes are driven by coupling of inertial waves and self-gravity, while the P and edge modes are driven by coupling of inertial waves across corotation. For the J, P and edge modes, corotation was usually located at or around the density maximum, while for the I+ (I-) modes corotation was found exclusively well outside (inside) of density maximum. J modes had barlike perturbed density eigenfunctions inside of the density max, and trailing spiral arms outside. I modes had barlike perturbed density eigenfunctions inside and outside of  $r_o$ , coupled by a trailing or leading spiral arm. P modes had bars near the inner edge of the disk which switched to both short and long trailing spiral arms outside of  $r_o$ . The instabilities with a large number of windings are referred to as edge modes.

We find that disks may be unstable to nonaxisymmetric modes, however high the Toomre  $Q$  parameter may be. For  $q = 2$  disks which formally have  $Q = 0$  disk systems are generally unstable dominated by  $m = 1$  modes over most of parameter space. Multi-armed modes,  $m \geq 2$  modes dominate only at large  $r_-/r_+$  for given  $M_*/M_d$  with only few exceptions. For small  $M_*/M_d$  and small  $r_-/r_+$  I modes dominate giving way to J modes at high  $r_-/r_+$ . At large  $M_*/M_d$ , I and then P modes dominate. Similar behavior is found for  $q = 1.75$  and 1.5 disks which can show  $Q > 2$  everywhere. We find, however, that the range over which  $m \geq 2$  modes dominate covers a larger portion of the parameter space. For  $q = 1.5$ , the region stretches to  $r_-/r_+ \sim 0.1$  for the disk mass range  $M_*/M_d \approx 1$  to 20. For protostellar and protoplanetary disks with near *Keplerian* rotation, disks with  $M_*/M_d \approx 1$  to 20, multi-armed modes,  $m = 2, 3$ , and 4 modes, dominate instability in contrast to  $q \sim 2$  disks which are dominated by one-armed modes.

The instability regimes of multi-armed modes in disks track the strength of self-gravity as measured by parameter  $p$ . The fastest growing instabilities, the J modes, are in the upper left hand corner of  $(r_-/r_+, M_*/M_d)$  space where  $p$  is largest. Growth rates decrease away from this corner, then increase and decrease forming a bulls eye pattern. Two stable regions where  $y_2$  goes to 0 are found. There is a short arc sweeping from  $r_-/r_+ \approx 0.425$ ,  $M_*/M_d = 0.01$  to  $r_-/r_+ \approx 0.475$ ,  $M_*/M_d = 0.05$ , and a long arc sweeping through parameter space from  $0.1 \leq r_-/r_+ \leq 0.20$ ,  $0.01 \leq M_*/M_d \leq 0.1$  to  $r_-/r_+ \approx 0.70$ ,  $17.5 \leq M_*/M_d = 50$ . The two arcs roughly follow  $p \approx 7.5$  and 3 breaking the parameter space into regions dominated by I modes and P/edge modes, respectively.  $y_1$  changes discontinuously between mode types, while  $y_2$  changes in a continuous manner.

We modeled torques driven by the Reynolds stress and gravitational stress that result from the development of nonaxisymmetric instability into the nonlinear regime using our linear eigenfunctions for comparison to the early stages of numerical simulations. For Jeans-like J modes, which dominate in the region of low star mass to disk mass ratios,  $M_*/M_d < 0.1-0.5$ , and wide disks,  $r_-/r_+ > 0.6-0.7$ , the disk torque is driven by the gravitational stress. For larger  $M_*/M_d$  and smaller  $r_-/r_+$  J modes give way first to I modes, where disk self-gravity and inertial effects are comparable with disk torques driven by both the gravitational and Reynolds stresses, and then to P and edge modes. These are dominated by the effects of shear except for one-armed P modes, where the star/disk coupling was sometimes dominant. For P and edge modes, disk torques are driven by the Reynolds stress except  $m = 1$  P modes.

Although illustrative, our work is incomplete as we did not investigate the saturation of the unstable modes in the nonlinear regime. We are currently pursuing this question through nonlinear simulations of unstable disk systems which include thermal effects such as entropy generation in shock waves and entropy loss through radiative cooling.

**Acknowledgements** The authors thank the National Science Foundation and the National Aeronautics and Space Administration for support. The computations were supported by a Major Research Instrumentation grant from the National Science Foundation, Office of Cyber Infrastructure, "MRI-R2: Acquisition of an Applied Computational Instrument for Scientific Synthesis (ACISS)," Grant Number OCI-0960534. The authors would like to thank an anonymous referee whose careful reading, and thoughtful comments and criticisms, greatly improved our manuscript. JNI thanks Kobe University and host, Dr. Masayuki Itoh, for support and hospitality during which a portion of this research was carried out.

## References

- Adams, F.C., Ruden S.P. & Shu F.H. 1989, *Astrophys. J.*, 347, 959
- Andalib, S.W., Tohline, J.E., & Christodoulou, D.M. 1997, *Astrophys. J. Suppl. Ser.*, 108, 471
- Armitage, P.J. 2011, *Annu. Rev. Astron. Astrophys.*, 49, 195
- Balbus, S. & Hawley, J. 1998, *RMP*, 70, 1
- Berio, D., Stee, Ph., Vakili, F., Mourard, D., Bonneau, D., Chesneau, O., Mignant, D., Thureau, N., & Hinata, R. 1999, *Astron. Astrophys.*, 345, 203
- Blaes, O. 1985, *Mon. Not. R. Astron. Soc.*, 216, 553
- Christodoulou, D.M. & Narayan, R. 1992, *Astrophys. J.*, 395, 451
- DeWarf, J., Eisloffel, J., Ray, T.P., Bacciotti, F., & Davis, C. 2003, *Astrophys. J.*, 590, 357
- Drazin, P.G. & Reid, W.H. 2004, *Hydrodynamic Stability*, (Cambridge Univ. Press: Cambridge)
- Durisen, R.H., Boss, A.P., Mayer, L., Nelson, A.F., Quinn, T., & Rice, W.K.M. 2007, *Protostars and Planets V* (prpl), eds. B. Reipurth, D. Jewitt, & K. Keil (Tucson: U Arizona Press), 609
- Dyson, F.W. 1893, *Trans. R. Soc. Lond. A*, 184, 43
- Eriguchi, Y. & Hachisu, I. 1983, *Progr. Theor. Phys.*, 69, 1131
- Fukugawa, M. *et al.* 2004, *Astrophys. J.*, 605, L17
- Goldreich, P., Goodman, J., & Narayan, R. 1986, *Mon. Not. R. Astron. Soc.*, 221, 339
- Goodman, J. & Narayan, R. 1988, *Mon. Not. R. Astron. Soc.*, 231, 97
- Hachisu, I. 1986 *Astrophys. J. Suppl. Ser.*, 61, 479
- Hachisu, I. & Eriguchi, Y. 1985a, *Astron. Astrophys.*, 143, 355
- Hachisu, I. & Eriguchi, Y. 1985b, *Astron. Astrophys.*, 147, 13
- Hadley, K.Z. & Imamura, J.N. 2011, *Astrophys. Space Sci.*, 334, 1
- Hadley, K.Z., Imamura, J.N., Keever, E., & Tumblin, R. 2014, *Astrophys. Space Sci.*, submitted
- Hashimoto, J. *et al.* 2011, *Astrophys. J.*, 729, L17
- Henning, T., Burkert, A., Launhardt, R., Leinert, C., & Stecklum, B. 1998, *Astron. Astrophys.*, 336, 565
- Heemskerk, M.H.M., Papaloizou, J.C., & Savonije, G.J. 1992, *Astron. Astrophys.*, 26
- Goldreich, P., Tremaine, S. 1979, *Astrophys. J.*, 233, 857
- Imamura, J.N., Durisen, R.H., & Pickett, B.K. 2000, *Astrophys. J.*, 528, 946
- Imamura, J.N., Toman, J., Durisen, R. H., Pickett, B., K., & Yang, S. 1995, *Astrophys. J.*, 444, 363
- Kato, S. 1983, *Publ. Astron. Soc. Jpn.*, 35, 249
- Kojima, Y. 1986, *Progr. Theor. Phys.*, 75, 251
- Kojima, Y. 1989, *Mon. Not. R. Astron. Soc.*, 236, 589
- Lai, D. 2001, *AIP conf.*, 575, 246
- Landau, L.D. & Lifshitz, E.M. 1987, *Fluid Mechanics*, Second Edition, (Pergamon Press: Oxford)
- Lin, M.-K., Krumholz, M.R., & Kratter, K.M. 2011, *Mon. Not. R. Astron. Soc.*, 416, 580
- Noh, H., Vishniac, E.T., & Cochran, W.D. 1992, *Astrophys. J.*, 397, 347
- Ogilvie, G.I. 2008, *Mon. Not. R. Astron. Soc.*, 388, 1372
- Okazaki, A.T. 1991, *Publ. Astron. Soc. Jpn.*, 43, 75
- Okazaki, A.T. 1997, *Astron. Astrophys.*, 318, 548
- Oppenheimer, B.R., Brenner, D., Hinkley, S., Zimmerman, N., Sivaramakrishnan, A., Soumerai, R., Kuhn, J., Graham, J.R., Perrin, M., Lloyd, J.P., Roberts, L.C., & Harrington, D.M. 2008, *Astrophys. J.*, 679, 1574
- Papaloizou, J.C.B. & Lin, D.N.C. 1989, *Astrophys. J.*, 344, 645
- Papaloizou, J.C.B. & Pringle, J.E. 1984, *Mon. Not. R. Astron. Soc.*, 208, 721
- Papaloizou, J.C.B. & Pringle, J.E. 1985, *Mon. Not. R. Astron. Soc.*, 213, 799
- Papaloizou, J.C.B. & Pringle, J.E. 1987, *Mon. Not. R. Astron. Soc.*, 225, 267
- Papaloizou, J.C.B. & Savonije, G.J. 1991, *Astron. Astrophys.*, 248, 353
- Papaloizou, J.C.B. & Savonije, G.J. 2006, *Astron. Astrophys.*, 456, 1097
- Papaloizou, J.C.B., Savonije, G.J. & Henrichs, H.F. 1992, *Astron. Astrophys.*, 265, 45
- Papaloizou, J.C.B. & Terquem, C. 2006, *Rep. Prog. Phys.*, 69, 119
- Pietu, V., Guilloteau, S., & Duitrey, A. 2005, *Astron. Astrophys.*, 443, 945
- Ryu, D. & Goodman, J. 1994, *Astrophys. J.*, 422, 269
- Shariff, K. 2009, *ARFDyn*, 41, 283
- Shu, F.H., Adams, D.C., & Lizano, S. 1987, *Annu. Rev. Astron. Astrophys.*, 25, 23
- Takami, H., Takata, N., Kanazawa, T., Hayano, Y., Kamata, Y., Gaessler, W., Minowa, Y., & Iye, M. 2002, *ESOC*, 58, 427
- Tanaka, T., Takeuchi, T., & Ward, W.R. 2002, *Astrophys. J.*, 565, 257
- Tassoul, J.-L. 1978, *Theory of Rotating Stars* (Princeton U. Press)
- Tohline, J.E. 2002, *Annu. Rev. Astron. Astrophys.*, 40, 349
- Tohline, J.E., & Hachisu, I. 1990, *Astrophys. J.*, 361, 394
- Toomre, J. 1964, *Astrophys. J.*, 139, 1217
- Vakili, F., Mourard, D., & Stee, Ph. 1994, in *Proc. of IAU Sym. 162: Pulsation, Rotation, and Mass Loss of Early Type Stars*, eds. L.A. Balona, H.F. Henrichs, & J.M. LeContel (Dordrecht: Kluwer Acad. Press), 435
- Vakili, F., Mourard, D., Stee, Ph., Bonneau, D., Berio, P., Chesneau, O., Thureau, N., Morand, F., Labeyrie, A., & Tallon-Bosc, I. 1998, *Astron. Astrophys.*, 335, 261
- Williams, H.A. & Tohline, J.E. 1987, *Astrophys. J.*, 315, 594
- Woodward, J.W. 1994, Ph. D. dissertation, Louisiana State University
- Woodward, J.W., Tohline, J.E., & Hachisu, I. 1994, *Astrophys. J.*, 420, 247
- Yuan, C. & Cassen, P. 1985, *Icarus*, 64, 435